Paleoceanography and Paleoclimatology

RESEARCH ARTICLE
10.1029/2021PA004361

Constraints on Marine Isotope Stage 3 and 5 Sea Level From the Flooding History of the Karimata Strait in Indonesia

Thomas L. Weiss[1,2], Braddock K. Linsley[1], Arnold L. Gordon[1,2], Yair Rosenthal[3,4], and Stefanie Dannenmann-Di Palma[5]

[1]Lamont-Doherty Earth Observatory of Columbia University, Palisades, NY, USA, [2]Department of Earth and Environmental Science, Columbia University, New York, NY, USA, [3]Department of Marine and Coastal Sciences, Rutgers University, State University of New Jersey, New Brunswick, NJ, USA, [4]Department of Earth and Planetary Sciences, Rutgers University, Busch Campus, Piscataway, NJ, USA, [5]United Nations Office for Disaster Risk Reduction, Brussels, Belgium

Abstract Global mean sea level (GMSL) during intermediate interglacial Marine Isotope Stage 3 (MIS 3) (60–26 ka) has proven difficult to constrain. Paleo-sea level estimates based on ice margin, modeling, and paleo-shoreline reconstructions indicate that MIS 3 GMSL was substantially higher than reconstructed from deep-ocean benthic foraminifera oxygen isotope ($\delta^{18}O$) and coral records, implying much smaller ice sheets during MIS 3. Here, we use the $\delta^{18}O$ and Mg/Ca chemistry of surface and thermocline dwelling foraminifera in the Sulu Sea in the western Pacific margin to estimate relative changes of the influx of South China Sea surface flow through the Sulu Sea over the last 140 ka. We show that this South China Sea throughflow is controlled in part by changes in GMSL modulating the depth of the 36 m deep Karimata Strait at the southern end of the South China Sea. We constrain maximum allowable GMSL at the beginning and end of MIS 3 to -22 ± 6 and -29 ± 5 m, respectively, and minimum allowable GMSL during interglacial stages MIS 5c and 5a (117–72 ka) to range from -3 ± 8 to -8 ± 8 m and -11 ± 7 to -12 ± 7 m, respectively. Our results constrain MIS 3 GMSL, but do not rule out higher MIS 3 ice margin, modeling, and paleo-shoreline-based MIS 3 GMSL estimates or lower coral and seawater $\delta^{18}O$-based estimates. Our results favor the highest MIS 5a and 5c GMSL estimates and confirm that the Sunda Shelf served as a land-bridge for human and megafauna migration during MIS 3 when humans first arrived in Borneo.

Key Points:

- Sulu Sea surface salinity records Karimata Strait inundation since 125 ka and in combination with strait depth, constrains sea level
- A subaerial Karimata Strait during Marine Isotope Stage 3 (MIS 3) may have aided human migration to Borneo and shows Global mean sea level (GMSL) was lower than -22 ± 3 m
- The Karimata Strait was inundated during MIS 5a and 5c, and GMSL was above -12 ± 7 m relative to today

Supporting Information:

Supporting Information may be found in the online version of this article.

Correspondence to:

T. L. Weiss,
tlw2130@columbia.edu

Citation:

Weiss, T. L., Linsley, B. K., Gordon, A. L., Rosenthal, Y., & Dannenmann-Di Palma, S. (2022). Constraints on marine isotope stage 3 and 5 sea level from the flooding history of the Karimata Strait in Indonesia. *Paleoceanography and Paleoclimatology*, *37*, e2021PA004361. https://doi.org/10.1029/2021PA004361

Received 14 SEP 2021
Accepted 20 JUL 2022

Author Contributions:

Conceptualization: Thomas L. Weiss, Braddock K. Linsley
Data curation: Thomas L. Weiss
Formal analysis: Thomas L. Weiss, Stefanie Dannenmann-Di Palma
Funding acquisition: Thomas L. Weiss, Braddock K. Linsley
Investigation: Thomas L. Weiss, Yair Rosenthal
Methodology: Thomas L. Weiss, Braddock K. Linsley
Resources: Braddock K. Linsley, Yair Rosenthal
Visualization: Thomas L. Weiss
Writing – original draft: Thomas L. Weiss

1. Introduction

Marine Isotope Stage 3 (MIS 3), considered a relatively warm transitional interglacial stage that lasted from 60 ka to the beginning of the Last Glacial Maximum (LGM; 26 ka), is characterized by highly variable climate, punctuated by repeated millennial-scale warming episodes, called Dansgaard-Oeschger events, during which the North Atlantic warmed 8°–15°C (Blunier et al., 1998). The extent and variability of continental ice sheets and global mean sea level (GMSL) during MIS 3 relative to the LGM and to the preceding interglacial (MIS 5), has been implicated in causing this climate variability (Siddall et al., 2008 and references therein) and remains controversial. Constraining MIS 3 GMSL is crucial for (a) evaluating how quickly ice sheets grew and sea level fell as global climate transitioned into the LGM (Dalton et al., 2019; Pico et al., 2017), (b) understanding ice sheet stability in the past, and (c) projecting future ice sheet melting because it precedes the LGM and is characterized by substantial climatic instability. It has proven difficult however, to constrain sea level during this interval (Pico et al., 2017; Siddall et al., 2008). Many studies have estimated global ice volume from foraminiferal $\delta^{18}O$ either by using paleo-reconstructions from regions where foraminiferal $\delta^{18}O$ is thought to be strongly correlated to ice volume (Rohling et al., 2008; Siddall et al., 2003, 2008) or by accounting for temperature using Mg/Ca based temperature compilations (Spratt & Lisiecki, 2016). These estimates generally suggest that peak MIS 3 sea level was −30 to −60 m relative to today (Rohling et al., 2008; Siddall et al., 2003, 2008; Spratt & Lisiecki, 2016). More direct coral and ice margin-based reconstructions are rare because shorelines are generally below modern sea level and glacial features were destroyed by subsequent ice sheet advance during the LGM (Siddall et al., 2008). Coral-based records do not show strong agreement, suggesting a wide range of maximum MIS 3 sea level of −30 to −80 m (Chappell, 2002; Chappell et al., 1996; Cutler et al., 2003; Hanebuth et al., 2006; Thompson, 2005; Thompson & Goldstein, 2006; Yokoyama et al., 2001). While these direct coral-based and indirect marine sediment core $\delta^{18}O$ records of GMSL summarized above indicate wide ranges of maximum MIS 3 GMSL, most tend toward lower GMSL (−60 to −80 m) (Chappell, 2002; Chappell et al., 1996; Cutler et al., 2003; Hanebuth et al., 2006; Siddall et al., 2008; Thompson, 2005; Thompson & Goldstein, 2006; Yokoyama et al., 2001).

Writing – review & editing: Thomas L. Weiss, Braddock K. Linsley, Arnold L. Gordon, Yair Rosenthal

More recent sea level and ice sheet extent studies have argued for higher MIS 3 sea level, suggesting substantially more rapid ice sheet growth from MIS 3 to the LGM. Pico et al. (2016) argue for peak MIS3 GMSL of -38 ± 7 m relative to today on the basis of Glacial Isostatic Adjustment (GIA) modeling and analysis of Yellow Sea sediment cores. A similar conclusion was reached by Pico et al. (2017) using modeling GIA simulations to show that peak MIS 3 GMSL of −40 m is consistent with paleo-shoreline indicators from the Albemarle Embayment in Virginia and North Carolina. Batchelor et al. (2019) estimate a comparable MIS 3 GMSL range based on their global compilation of Pleistocene ice sheet margin indicators, as do Gowan et al. (2021) who use a combination of ice sheet margin indicators and modeling. Accurate understanding of MIS 3 sea level is crucial, given (a) the importance of understanding rates of ice sheet growth as Earth's climate transitioned into the LGM, (b) how rapid climatic variability during MIS 3 impacted sea level, and (c) the ubiquitous use of stacked benthic foraminifera $\delta^{18}O$ composites as a indicators of ice volume and sea level. It is therefore clear that more research is needed to determine whether MIS 3 sea level is better represented by lower coral and foraminiferal $\delta^{18}O$-based estimates (Chappell, 2002; Cutler et al., 2003; Hanebuth et al., 2006; Siddall et al., 2008; Spratt & Lisiecki, 2016; Thompson, 2005; Thompson & Goldstein, 2006) or more recent high GIA modeling, shoreline, and ice sheet margin indicator-based estimates (Batchelor et al., 2019; Pico et al., 2016, 2017).

While coral and foraminiferal $\delta^{18}O$-based estimates of MIS 3 sea level vary widely, they almost universally agree that MIS 3 sea level was substantially lower (generally >40 m lower) than MIS 5a–5d (72–117 ka), the previous warm period (Dalton et al., 2019; Siddall et al., 2008; Spratt & Lisiecki, 2016; Thompson, 2005; Thompson & Goldstein, 2006). In contrast, more recent GIA modeling, shoreline, and ice sheet margin indicator-based estimates suggest MIS 3 and MIS 5a–5d sea level were much more similar, with MIS 3 sea level only ∼20 m below MIS 5a–5d (Batchelor et al., 2019; Pico et al., 2016, 2017). Previously published $\delta^{18}O$ results from Sulu Sea sediment cores generated using the surface-dwelling foraminifera *G. ruber* have been proposed to accurately reflect variations in sea level based on their near identical scaling of glacial-interglacial variability with benthic foraminifera $\delta^{18}O$ stacks (Dannenmann et al., 2003; Linsley, 1996; Oppo et al., 2003b; Rosenthal et al., 2003a). The most obvious departure from this trend however occurs during MIS 3, when Sulu Sea *G. ruber* $\delta^{18}O$ in MD97-2141 and Ocean Drilling Program Site 769A is nearly equivalent to MIS 5a–5d (Dannenmann et al., 2003; Linsley, 1996; Oppo et al., 2003b; Rosenthal et al., 2003a) (Figures 1 and 2). The surface mixed-layer foraminifera $\delta^{18}O$ record from the Sulu Sea appears to support more recent GIA modeling and ice margin-based reconstructions of MIS3 sea level, but foraminiferal $\delta^{18}O$ is controlled by a combination of temperature and local seawater $\delta^{18}O$ ($\delta^{18}O_w$) which is a function of global ice volume/sea level effects on global ocean $\delta^{18}O_w$ and local salinity. Because the Sulu Sea is a marginal basin located in the center of the Indo-Australian Monsoon Region, any surface ocean-based foraminiferal shell $\delta^{18}O$ record is susceptible to changes in local temperature and salinity potentially obscuring the sea level signal (Figure 1).

In order to isolate the sea level signal in the Sulu Sea *G. ruber* $\delta^{18}O$ record, we reconstruct water temperature variability by extending the previously existing *G. ruber* Mg/Ca-based temperature record from Sulu Sea core MD97-2141 to the beginning of MIS 5e (132 ka). We use the *G. ruber* $\delta^{18}O$ and Mg/Ca based temperature records to calculate a surface ocean $\delta^{18}O_w$ record which primarily reflects ice volume/sea level effects on global ocean $\delta^{18}O_w$ and local salinity. Lastly, we generate $\delta^{18}O$ and Mg/Ca records spanning MIS 3 to MIS 5d using the thermocline dwelling foraminifera *G. tumida* (calcification depth in the Sulu Sea 100–130 m from Weiss et al. (2021b)) from the same core and derive a $\delta^{18}O_w$ reconstruction that reflects both ice volume/sea level effects on global ocean $\delta^{18}O_w$ and local thermocline salinity. Sulu Sea thermocline and surface salinity are controlled by different mechanisms (Gordon et al., 2011, 2012; Weiss et al., 2021b), whereas ice volume/sea level effects on $\delta^{18}O_w$ are global in nature and affect the Sulu Sea surface and thermocline equally. We are therefore able to use any differences between our *G. ruber* surface and *G. tumida* thermocline $\delta^{18}O_w$ records to deconvolve the *G. ruber* $\delta^{18}O_w$ record into its component local surface salinity and global ice volume fractions during MIS 3 and determine whether the global ice volume fraction is consistent with higher or lower MIS 3 sea level estimates.

1.1. Environmental Setting and Controls on Sulu Sea Surface and Thermocline $\delta^{18}O$

IMAGES core MD97-2141 is a 36 m giant piston core collected as part of the IPHIS-IMAGES III cruise of the R/V Marion Dufresne in May 1997 at 08°78'N, 121°28'E and 3,633 m water depth. Due to the shallow depth of the sills surrounding the Sulu Sea, deepwater ventilation is limited and a deep lysocline (∼3,800 m) leads to excellent carbonate preservation (Miao et al., 1994).

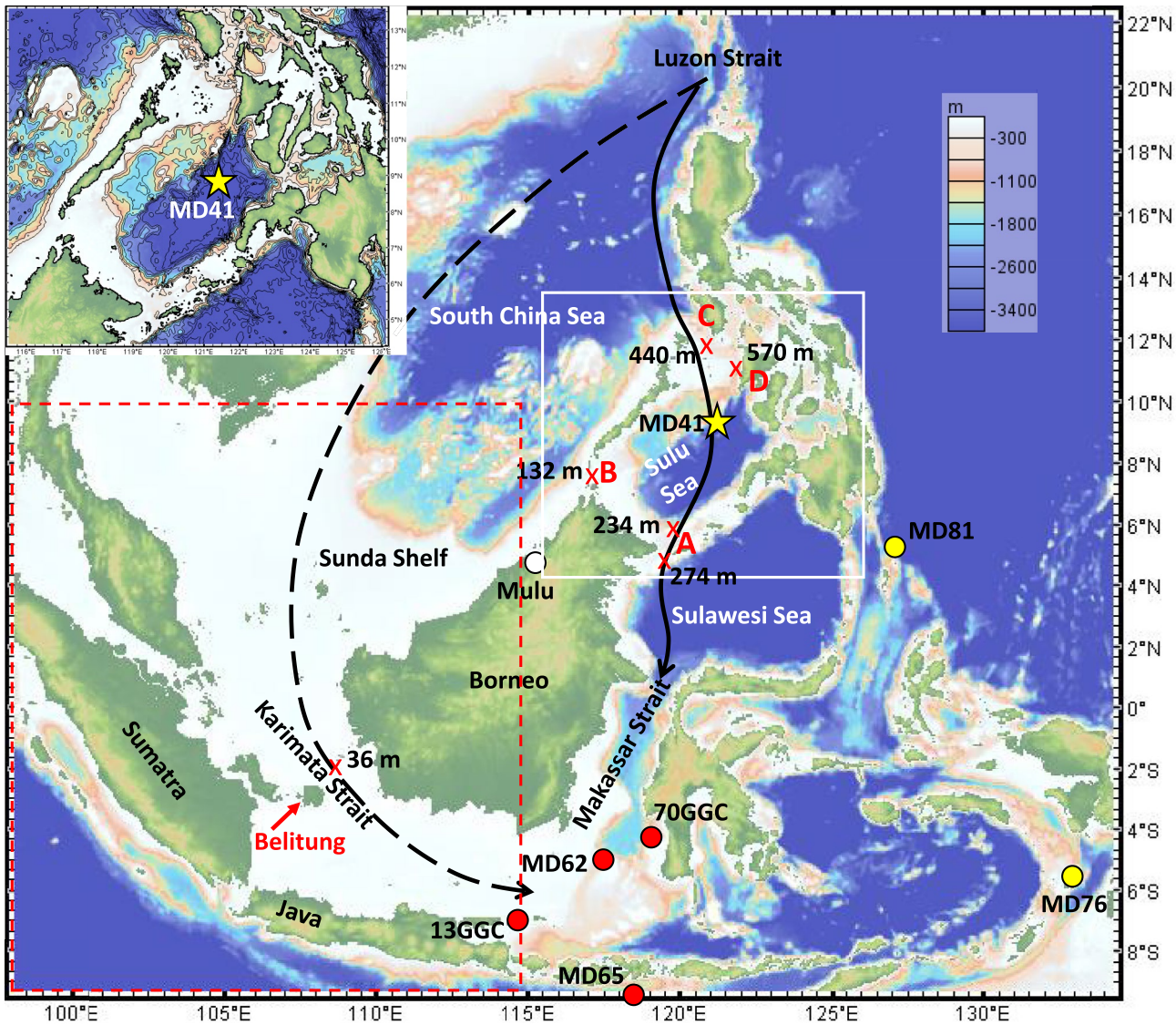

Figure 1. The Sulu Sea and marginal Indonesian Seas. (a) Sibutu Passage. (b) Balabac Strait, (c) Mindoro Strait, and (d) Panay Strait. Figure was made using the GeoMapApp: http://www.geomapapp.org (Ryan et al., 2009). Black lines indicate flow paths from the South China Sea. The dashed path only exists when the Karimata Strait is open. Locations of sediment cores north (upstream) of the Karimata Strait from Linsley et al. (2010) are marked in yellow and cores south (downstream) of the strait are marked in red. MD97-2141 is labeled as MD41 for shorthand. The location of Gunung Mulu National Park where Borneo speleothems were collected (Carolin et al., 2016b) is indicated in white. Belitung Island is marked in red (Sarr et al., 2019). Bathymetry in the white box is shown in the inset map. Bathymetry in the red dashed box is shown in Figure S1 in Supporting Information S1.

Modern Sulu Sea surface salinity is only very weakly correlated to local precipitation (r-value = 0.06) (Weiss et al., 2021b) but is instead dominated by the salinity of advected water from the South China Sea (Miao et al., 1994). South China Sea surface water mixes with monsoonal runoff to produce relatively fresh surface salinity of 33 (Miao et al., 1994), before exiting the South China Sea via two routes. Approximately 1.62 Sv of South China Sea surface water enters the Sulu Sea through the shallow Balabac (132 m) and Mindoro (440 m) Straits to the southeast before exiting the Sulu Sea through the Sibutu Passage (234 m) into the Sulawesi Sea and the northern Makassar Strait (Gordon et al., 2012; Miao et al., 1994). The remaining ~0.74 Sv of South China Sea outflow moves over the Sunda Shelf to the southwest, through the shallow Karimata Strait (Wang et al., 2019) which has a maximum depth of ~36 m (NOAA National Geophysical Data Center, 2009) (Figures 3a and 3b; Figure S2 in Supporting Information S1), and into the southern Makassar Strait (Xu et al., 2021). As a result of the advection of relatively fresh surface water from the South China Sea, the Sulu Sea surface is relatively fresh as well, with a salinity of ~34 (Miao et al., 1994) and the southern Makassar Strait freshens from ~34 during the

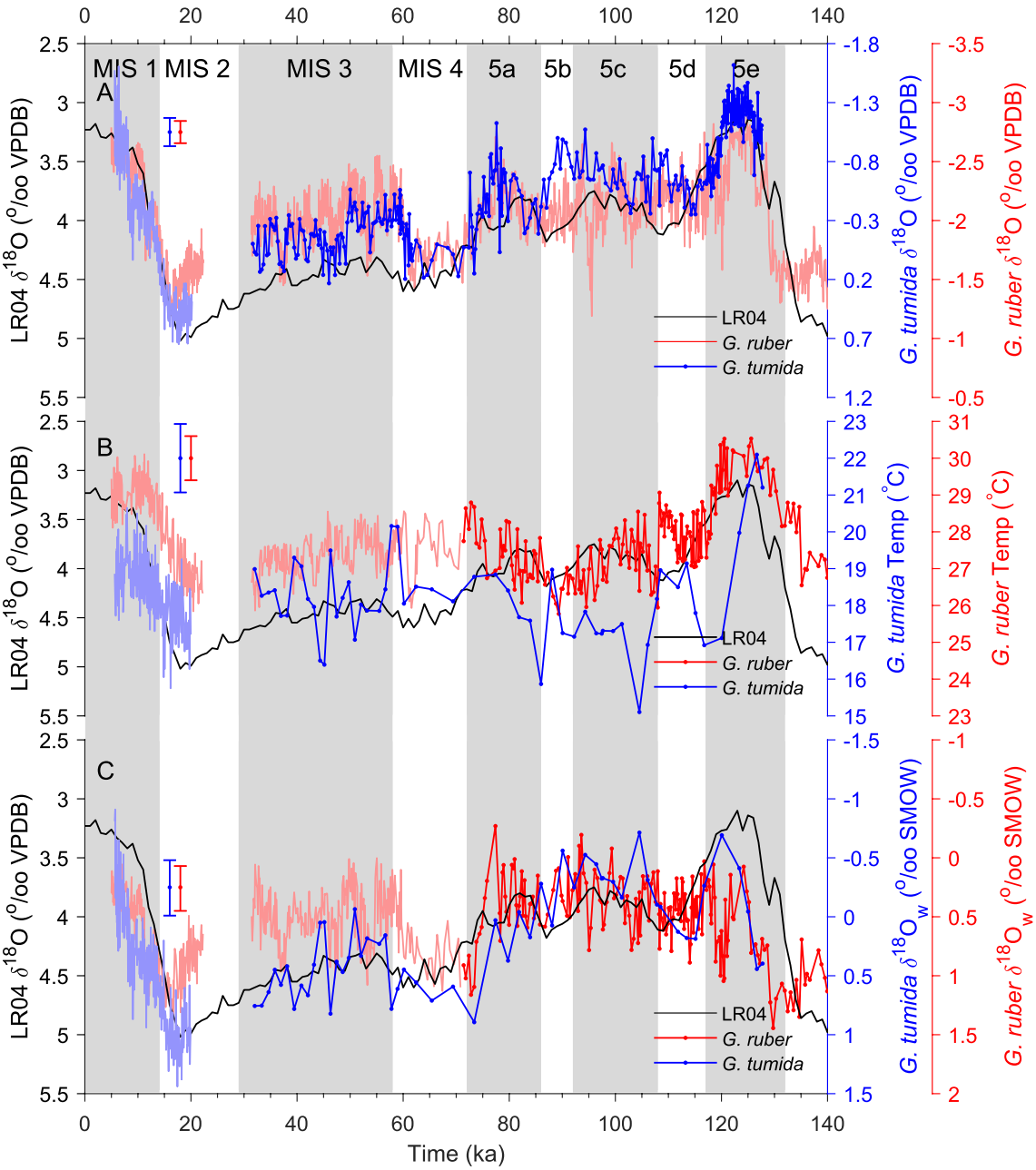

Figure 2. (a) Lisiecki and Raymo (2005) benthic $\delta^{18}O$ stack (LR04 Stack) (black), Sulu Sea *G. ruber* $\delta^{18}O$ (Dannenmann et al., 2003; Oppo et al., 2003b; Rosenthal et al., 2003a) (red), and Sulu Sea *G. tumida* $\delta^{18}O$ (blue). (b) Lisiecki and Raymo (2005) benthic $\delta^{18}O$ stack (black), Sulu Sea *G. ruber* Mg/Ca based temperature (Dannenmann et al., 2003; Oppo et al., 2003b; Rosenthal et al., 2003a) (red), and Sulu Sea *G. tumida* Mg/Ca based temperature (blue). (c) Lisiecki and Raymo (2005) benthic $\delta^{18}O$ stack (black), Sulu Sea *G. ruber* $\delta^{18}O_w$ (Dannenmann et al., 2003; Oppo et al., 2003b; Rosenthal et al., 2003a) (red), and Sulu Sea *G. tumida* $\delta^{18}O_w$ (blue). The light red and blue data were previously published, whereas the dark red and blue are published by this study.

summer to ~32 during the winter when flow through the Karimata Strait is strongest (Gordon & Villanoy, 2011; Linsley et al., 2010).

The Karimata Strait is far shallower than the Balabac and Mindoro Straits, so whenever sea level is below the depth of the 36 m Karimata Strait, the only outlet from the South China Sea for relatively fresh surface water is into the Sulu Sea and any water that would have flowed into the Karimata Strait is redirected there (Linsley et al., 2010). Paleoclimate records show that under these conditions, the redirection of Karimata Strait throughflow into the Sulu Sea leads the South China Sea to impart an even stronger influence on Sulu Sea surface

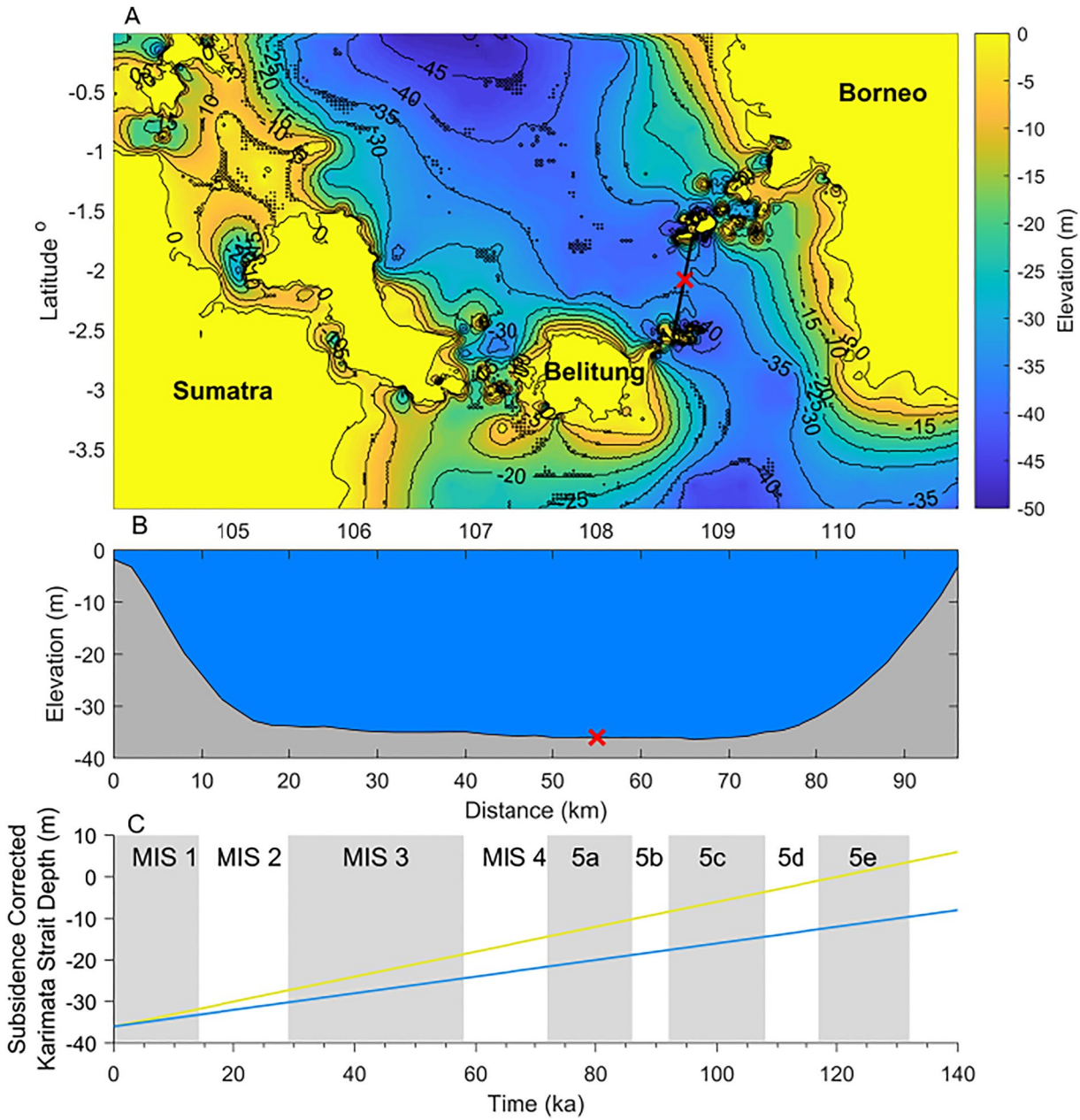

Figure 3. (a) Contour map of the modern Karimata Strait. Bathymetry data are from the ETOPO1 Global Relief Model (NOAA National Geophysical Data Center, 2009; The NOAA Technical Memorandum, 2009). (b) Cross section of the Karimata Strait along the black line from (a). (c) Topographic depth of the Karimata Strait (location marked with red x in panels a and b) corrected through time using the maximum (yellow) and minimum (light blue) subsidence rates from Sarr et al. (2019).

salinity, freshening it even more than it presently does (Linsley et al., 2010; Rosenthal et al., 2003a). Linsley et al. (2010) show an increase in salinity at ~9.5 ka in core MD97-2141 and several other cores located in the Northern Hemisphere of the far western equatorial Pacific relative to several cores south of the strait (see core locations in Figure 1). They argue that opening of the Karimata Strait at ~9.5 ka due to rising sea level siphoned relatively freshwater away from the Sulu Sea. This weakened the Sulu Sea's connection with the South China Sea and increased its surface salinity, while delivering that relatively freshwater to the cores south of the Karimata Strait and freshening the Southern Makassar Strait. Rosenthal et al. (2003a) reported that a reduced amplitude LGM to Holocene $\delta^{18}O_w$ signal in the Sulu Sea mixed layer resulted from a relatively fresh Sulu Sea Surface during the LGM due to a closed Karimata Strait and strengthened connection between the Sulu Sea surface and

South China Sea when sea level was substantially lower. Climate modeling shows that closing of the Karimata Strait also freshens the South China Sea surface through circulation changes (Di Nezio et al., 2016) and this would then be translated to the Sulu Sea surface.

Sulu Sea thermocline salinity is controlled by entirely different mechanisms than the surface. Density driven limitations on vertical mixing prevent local precipitation from influencing the Sulu Sea thermocline (Weiss et al., 2021b). Furthermore, sea level driven opening and closing of the Karimata Strait should not affect the Sulu Sea thermocline as it is substantially deeper than the strait, beginning below ~50 m water depth, and physical limitations would prevent this signal from mixing into the thermocline as well (Gordon & Villanoy, 2011; Weiss et al., 2021b). This is demonstrated by the Sulu Sea thermocline LGM to Holocene $\delta^{18}O_w$ amplitude which is not reduced like it is in the Sulu Sea surface, indicating the thermocline was not freshened by the closed Karimata Strait during the LGM (Rosenthal et al., 2003a; Weiss et al., 2021b).

Instead, instrumental records show that Sulu Sea thermocline salinity is strongly controlled by the bifurcation latitude of the North Equatorial Current (*r*-value ranges from 0.53 to 0.62 and from 85 to 165 m water depth) which controls the flow of relatively salty water into the Sulu Sea thermocline from the western Pacific through the Luzon Strait and South China Sea by modulating the strength of the Kuroshio Current (Weiss et al., 2021b). The North Equatorial Current bifurcation latitude does not affect Sulu Sea surface salinity (*r*-value ranges from 0.00 to −0.004 above 35 m) (Weiss et al., 2021b). *G. tumida* based $\delta^{18}O_w$ records from core MD97-2141 show that Sulu Sea thermocline salinity was strongly influenced by the North Equatorial Current bifurcation latitude from the LGM to the early Holocene and therefore responded somewhat differently to climate variability than surface salinity (Weiss et al., 2021b).

2. Methods

2.1. Age Model

The age model for core MD97-2141 is based on radiocarbon dates of surface-dwelling planktonic foraminifera from ~4 to 40 ka and orbital tuning for older sections of the core and was originally published in de Garidel-Thoron et al. (2001) and later used in Dannenmann et al. (2003), Oppo et al. (2003b), and Rosenthal et al. (2003a). Weiss et al. (2021b) recalibrated the original dates and updated the original age model for sections younger than ~22 ka. We extended the updated age model to ~41 ka by recalibrating four more radiocarbon dates using the Marine13 calibration curve from CALIB 7.04 and following the same methods as Weiss et al. (2021b) (Table S1 in Supporting Information S1). As there is minimal difference between the new and old calibrations of the oldest radiocarbon date (47 years) we apply the original orbitally tuned age model to samples older than the oldest recalibrated radiocarbon date. The updated age model uses the default CALIB 7.04 time-dependent reservoir correction of ~400 years and has radiocarbon tie-point calibration errors of 51–245 years.

2.2. Stable Isotopes and Trace Metals

Core MD97-2141 was slab sampled in 1 cm increments. For this study, *G. tumida* stable isotopes were analyzed every fifth cm (376 samples at ~0.3 kyr resolution) and *G. tumida* trace metals every 20th cm (60 new samples at ~1.5 kyr resolution). *G. tumida* stable isotopes were analyzed at lower temporal resolution than *G. ruber* because we were primarily interested in the comparison between MIS 5 and MIS 3 and did not need to capture high resolution variability. *G. tumida* trace metals were run in even lower resolution because our stable isotope analyses had already shown that higher resolution analyses were not necessary to compare MIS 5 and MIS 3. Eleven *G. tumida* in the 400–600 size fraction were picked for each sample for stable oxygen isotope analysis ($\delta^{18}O$) and eleven (22 total *G. tumida* per sample) more for Mg/Ca analysis. All foraminifera were viewed under a Keyence VHX-5000 Digital Microscope at high magnification (100–200x) to ensure specimens were clean, conformed to the stereotypical *G. tumida* morphotype, and lacked secondary calcification. The maximum-area-measurement application on the digital microscope was also used to confirm size of the individuals. Any specimen that was not deemed pristine or did not fall into the proper size fraction when measured using the Keyence digital microscope was not geochemically analyzed. Where a sample did not have 11 individual foraminifera that met selection criteria, specimens were pooled from adjacent 1 cm interval samples and an average age for all pooled samples was assigned.

To reduce selective loss of fine test fragments that could bias geochemical results, foraminifera were not cleaned prior to stable isotope analysis. Each set of 11 foraminifera were crushed and homogenized and 50–80 µg

of fragments were randomly selected for stable isotope analysis. *G. tumida* shell $\delta^{18}O$ was analyzed at the Lamont-Doherty Earth Observatory (LDEO) Stable Isotope Lab using a Thermo DeltaV + mass spectrometer with a Kiel IV autosampler device. Results are reported in per mil (‰) versus Pee Dee Belemnite. The international standard NBS-19 was analyzed after every ninth sample and had a standard deviation of 0.06‰ for $\delta^{18}O$. Approximately 10% of all samples were run in replicate sourced from the same crushed and homogenized fragments and replicates had an average difference of 0.12‰ for $\delta^{18}O$.

At each sample depth, all 11 *G. tumida* individuals selected for trace metal analysis (~500 µg) were gently cracked open and cleaned following the methods of Yu et al. (2005) which involves a reductive cleaning in a solution of hydrazine, citric acid, and ammonium hydroxide to remove metal oxides, followed by an oxidative cleaning step using a solution of sodium hydroxide and hydrogen peroxide to remove organics. Cleaned fragments were dissolved in trace metal clean 0.065N HNO_3 (OPTIMA®) and analyzed for trace metal concentrations at the LDEO Trace Metal Lab using a ThermoScientific iCAPQ Q-ICP-MS in conjunction with a HEPA-filtered enclosed autosampler. For each sample, an aliquot was first analyzed to determine its Ca concentration and samples were diluted with trace metal clean 0.065N HNO_3 (OPTIMA®) to ~50 ppm Ca for final analyses. Prior to each sample run, eight standards with a range of trace metal ratios were analyzed to calibrate sample analyses. Sample results were corrected for drift using a standard bracketing every 10 samples and corrected for instrument noise and contamination using two blanks every sample run. Analytical precision (relative standard deviation) based on three standards analyzed for every ~9 samples was ≤0.56% for Mg/Ca. Approximately 10% of samples were run in replicate and had a root mean squared deviation of 3.48% for Mg/Ca.

Following the methods of Schmidt et al. (2004), cleaning efficacy for *G. tumida* Mg/Ca was determined by monitoring Fe/Ca, Al/Ca, and Mn/Ca. Data points at 102.88 and 110.15 ka were removed from the data set for having anomalously high Al/Ca (>50 µmol/mol) and the data point at 121.72 ka was removed for having anomalously high Mn/Ca (>800 µmol/mol). With these points removed, Fe/Ca, Al/Ca, and Mn/Ca all show low correlation to Mg/Ca ($r^2 < 0.2$). Data points at 54.35 and 118.43 ka had low Mg/Ca and were not included in the data set as low Ca concentrations (<10.5 ppm) suggested little to no sample material survived the cleaning process. Four other data points (44.35, 45.15, 86, and 104.54 ka) demonstrate low Mg/Ca that lead us to question the fidelity of their analysis. However, we did not remove them from the data set as they do not show anomalous values for any other trace metal.

G. ruber Mg/Ca from core MD97-2141 spanning ~4–135 ka was analyzed at Rutgers University using a Finnigan MAT Element Sector Field ICP-MS. Data from ~4 to 22 ka were published in Rosenthal et al. (2003a) and from ~31 to 70 ka in Dannenmann et al. (2003). There is a sedimentary hiatus in the core between ~22 and 31 ka. Here, we publish the rest of the *G. ruber* Mg/Ca record extending to 135 ka (see Table S2 in Supporting Information S1 for a breakdown of new vs. old data). A more detailed description of analytical methods is contained in the original publications (Dannenmann et al., 2003; Rosenthal et al., 2003a), however in short, 80 individual tests in the 212–300 µm size fraction were picked for each sample, crushed and rinsed in deionized water and methanol, then washed using an oxidizing solution followed by multiple weak acid leaches. Due to differences in lab procedures, *G. ruber* samples were not reductively cleaned prior to Mg/Ca analyses. While reductive cleaning may reduce *G. tumida* Mg/Ca by ~10% (Barker et al., 2003), we do not account for the offset to remain consistent with previously published data and because the different cleaning methods do not significantly affect the relative variability within each species and therefore do not affect our interpretations. Dannenmann et al. (2003) estimate external precision of ±1.2% based on repeated analysis of three consistency standards. Average standard error (1σ) for Mg/Ca replicates was ±0.12 mmol/mol.

Past mid-thermocline water temperature was calculated from *G. tumida* Mg/Ca using the Anand et al. (2003) multispecies calibration. Temperatures calculated from this calibration result in appropriate depth habitat estimates, relative variability is comparable to other species-specific calibrations (Hollstein et al., 2017), and the error estimate is more appropriate than the Hollstein et al. (2017) error estimate which is not species specific (Weiss et al., 2021b). We assume no salinity influence on *G. tumida* or *G. ruber* Mg/Ca as Sulu Sea salinity (Weiss et al., 2021b) is below the threshold of 35 where those effects are suggested to begin (Arbuszewski et al., 2010; Mathien-Blard & Bassinot, 2009). Seawater $\delta^{18}O$ ($\delta^{18}O_w$) was calculated from *G. tumida* Mg/Ca based temperature and $\delta^{18}O$ using the Bemis et al. (1998) low light *O. universa* calibration. Standard error for Mg/Ca based temperature and $\delta^{18}O_w$ were calculated following the methods of Mohtadi et al. (2014) using reproducibility. They average 0.93°C and 0.23‰, respectively. Sea surface temperature

was calculated from *G. ruber* Mg/Ca using the same calibration as Dannenmann et al. (2003) and Rosenthal et al. (2003a). This calibration is based on that of Rosenthal and Lohmann (2002) and utilizes foraminiferal test size-normalized shell weight to adjust for dissolution. Core top *G. ruber* Mg/Ca accurately reproduces modern local surface water temperature, supporting the validity of the calibration (Dannenmann et al., 2003). Furthermore, relative temperature variability is essentially the same between this calibration and Dekens et al. (2002) and Gray and Evans (2019) calibrations. Dannenmann et al. (2003) estimate a temperature error of ±0.6°C. We estimate the same error for the newly published *G. ruber* Mg/Ca based temperature data. We use the Bemis et al. (1998) low light *Orbulina universa* calibration to calculate surface $\delta^{18}O_w$ from newly published *G. ruber* Mg/Ca based temperature and previously published $\delta^{18}O$ as this is the method applied by Dannenmann et al. (2003) and Rosenthal et al. (2003a) for previously published $\delta^{18}O_w$ data (Dannenmann et al., 2003; Rosenthal et al., 2003a) and this will allow for the best comparison between *G. ruber* and *G. tumida* $\delta^{18}O_w$ data. Following the methods of Mohtadi et al. (2014) and using a temperature error of 0.6°C and average difference between $\delta^{18}O$ replicates of 0.094‰, we estimate *G. ruber* $\delta^{18}O_w$ error to average 0.18‰.

3. Results

3.1. Sulu Sea MIS 3 $\delta^{18}O_w$ Variability

In contrast to Sulu Sea $\delta^{18}O$ from surface dwelling *G. ruber*, our new $\delta^{18}O$ record from thermocline dwelling *G. tumida* from the same core shows substantially higher $\delta^{18}O$ during MIS 3 than during MIS 5a–5d, scaling well with relative variability between those two intervals in the LR04 benthic isotope record (see Figure 2a). Our extended Sulu Sea *G. ruber* and new *G. tumida* Mg/Ca-based temperature records demonstrate that there was little change in surface and thermocline temperatures in the Sulu Sea from MIS 5a–5d to MIS 3 (Figure 2b). As a result, the decrease in *G. ruber* derived surface $\delta^{18}O_w$ moving from MIS 4 into MIS 3 is larger than the concurrent decrease in *G. tumida* $\delta^{18}O_w$. The $\delta^{18}O_w$ records therefore show that while *G. ruber* derived Sulu Sea surface $\delta^{18}O_w$ was approximately the same during MIS 3 and MIS 5a–5d, *G. tumida* derived thermocline $\delta^{18}O_w$ during MIS 3 was more than 0.4‰ greater than during MIS 5a–5d, nearly double the propagated analytical and calibration error (Figure 2c and Figure S3 in Supporting Information S1).

Given the global nature of ice volume driven $\delta^{18}O_w$ variability, we can assume that both *G. ruber* in the Sulu Sea surface and *G. tumida* in the thermocline were exposed to the same ice volume driven $\delta^{18}O_w$ signal and it contributed equally to the surface and thermocline decreases in *G. ruber* and *G. tumida* $\delta^{18}O_w$ moving into MIS 3. Therefore, the larger magnitude of the decrease in *G. ruber* derived surface $\delta^{18}O_w$ from MIS 4 to MIS 3 must have been the result of a local surface freshening increasing the amplitude of the event in the surface ocean, a local increase in thermocline salinity reducing the amplitude in the thermocline, or some combination of both. Because Sulu Sea *G. tumida* derived thermocline $\delta^{18}O_w$ largely tracks the LR04 benthic isotope record and could thus be explained entirely by global ice volume $\delta^{18}O_w$ variability, we conclude that the *G. tumida* derived Sulu Sea thermocline $\delta^{18}O_w$ was not affected by local changes in thermocline salinity. Instead, we argue that the Sulu Sea surface was exposed to substantial local freshening during MIS 3 that greatly decreased *G. ruber* derived surface $\delta^{18}O_w$, resulting in approximately equal Sulu Sea surface $\delta^{18}O_w$ during MIS 3 and MIS 5. Such a conclusion disproves our hypothesis that similar $\delta^{18}O_w$ in the Sulu Sea surface during MIS 3 and MIS 5a–5d was the result of ice volume related global $\delta^{18}O_w$ variability and instead is consistent with the widely held interpretation of the LR04 benthic stack that global $\delta^{18}O_w$ was substantially higher during MIS 3 than MIS 5a–5d (Lisiecki & Raymo, 2005).

Along with the departure from the LR04 benthic stack observed in the *G. ruber* derived Sulu surface $\delta^{18}O_w$ record during MIS 3, we also see slightly reduced values during MIS 4, do not see any evidence of the MIS 5d (117–108 ka) and 5b (92–86 ka) cold intervals in the Sulu Sea *G. ruber* $\delta^{18}O_w$ record, and observe elevated $\delta^{18}O_w$ values from ~123 to 119 ka during the later portion of MIS 5e. We interpret slightly elevated *G. ruber* derived Sulu Sea surface ocean $\delta^{18}O_w$ relative to *G. tumida* derived thermocline $\delta^{18}O_w$ and the LR04 benthic stack during MIS 4 to be the result of local surface freshening because it is only observed in the *G. ruber* record. We interpret the absence of an increase in *G. ruber* derived Sulu surface $\delta^{18}O_w$ during MIS 5d and 5b (when we do see increases in the LR04 stack) to be the result of local surface freshening as well. Elevated values in *G. ruber* derived Sulu surface $\delta^{18}O_w$ from ~123 to 119 ka are not present in either the LR04 stack or the *G. tumida* derived thermocline record and we attribute them to a local increase in surface salinity.

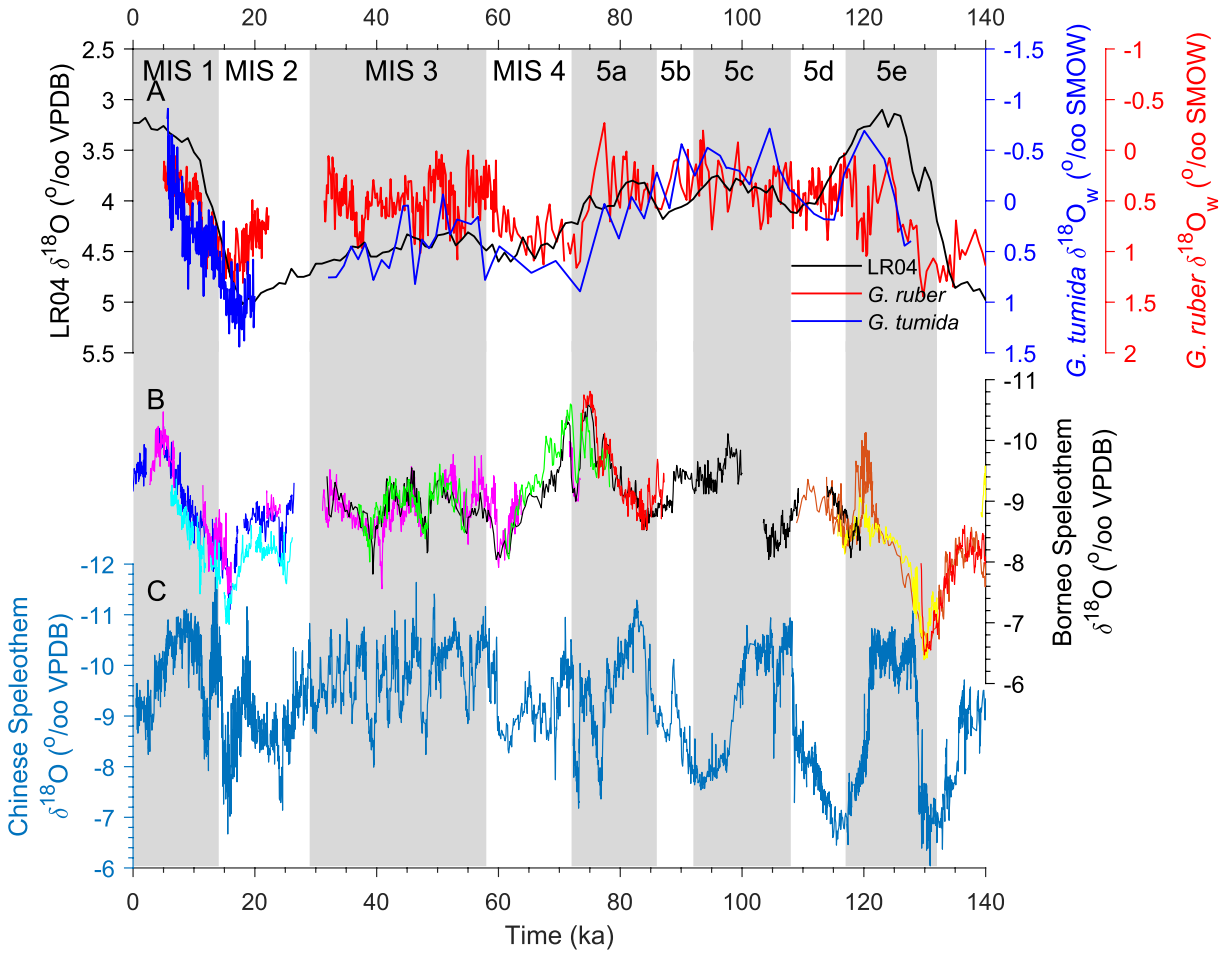

Figure 4. (a) Lisiecki and Raymo (2005) benthic $\delta^{18}O$ stack (black), Sulu Sea *G. ruber* $\delta^{18}O_w$ (Dannenmann et al., 2003; Oppo et al., 2003b; Rosenthal et al., 2003a) (red), and Sulu Sea *G. tumida* $\delta^{18}O_w$ (blue). (b) Ice volume corrected Borneo speleothem $\delta^{18}O$ (Carolin et al., 2016b). (c) Chinese speleothem $\delta^{18}O$ (Cheng et al., 2016). Data are ice volume corrected following the same method as Carolin et al. (2016b).

4. Discussion

4.1. Possible Origins of Sulu Surface Salinity Variability

Based on modern environmental conditions and previous Sulu Sea studies (Rosenthal et al., 2003a; Weiss et al., 2021b), we identify two likely drivers for freshening in the Sulu Sea during MIS 3 that would affect the surface and *G. ruber* shell chemistry, but would not be recorded by thermocline dwelling *G. tumida* as physical limitations on mixing would not allow them to reach that depth. The first potential driver is an increase in regional precipitation due to a strengthened Asian Monsoon during MIS 3 that could have freshened the Sulu Sea surface but would not mix to the depth habitat of *G. tumida* of 100–13 m (Weiss et al., 2021b). The second is a closed Karimata Strait that would have increased the delivery of relatively freshwater from the South China Sea to the Sulu Sea, bringing Sulu Sea surface salinity even closer to the salinity of the slightly fresher South China Sea. To compensate for higher global $\delta^{18}O_w$ during MIS 3 due to ice volume, precipitation would have had to be substantially greater during MIS 3 than during MIS 5a–5d. Ice volume corrected speleothem $\delta^{18}O$ records located proximally to the Sulu Sea on the island of Borneo indicate that this was not the case, suggesting that regional precipitation was roughly equivalent during MIS 3 and MIS 5a–5d (Carolin et al., 2016b) (Figure 4b). Ice volume corrected Chinese speleothem $\delta^{18}O$ indicates the same was true for the Chinese Monsoon (Cheng et al., 2016) (Figure 4c). We therefore conclude that the apparent freshening in the Sulu Sea surface during MIS 3 cannot be attributed to changes in the strength of the Asian Monsoon. Along similar lines, we do not observe evidence of an increase in precipitation during MIS 4, 5b, or 5d that could have decreased *G. ruber* derived Sulu Sea surface $\delta^{18}O_w$ (Carolin et al., 2016b; Cheng et al., 2016) (Figures 4b and 4c). Because speleothem

$\delta^{18}O$ paleohydrology reconstructions do not demonstrate a reduction in precipitation from ~123 to 119 ka (MIS 5e), but instead demonstrate a precipitation maximum during MIS 5e (Carolin et al., 2016b; Cheng et al., 2016) (Figures 4b and 4c), increased *G. ruber* derived Sulu surface $\delta^{18}O_w$ from ~123 to 119 ka also cannot be attributed to changes in precipitation.

4.2. Sunda Shelf Inundation History

4.2.1. The Karimata Strait as the Driver of Sulu Sea Surface Salinity

Having ruled out an increase in regional precipitation as the driver of Sulu Sea surface freshening during MIS 3 (Carolin et al., 2016b; Cheng et al., 2016) (Figures 4b and 4c), we instead attribute Sulu Sea surface freshening to a closed Karimata Strait during that period. We hypothesize that analogous to today, during much of MIS 5 sea level was high enough for the Karimata Strait to be open and siphon a portion of the low salinity South China Sea outflow away from the Sulu Sea. This reduced the freshening effect the South China Sea had on the Sulu Sea and produced relatively salty conditions in the Sulu Sea surface. We further hypothesize that in contrast to MIS 5, sea level during MIS 3 was lower relative to the Karimata Strait and the strait was closed, diverting all relatively fresh South China Sea outflow into the Sulu Sea and freshening the Sulu Sea surface enough that *G. ruber* $\delta^{18}O_w$ during MIS 3 was the same as during MIS 5a–5d.

4.2.2. Karimata Strait Flooding Record

The Karimata Strait appears to have opened for the first time post-MIS 6 at ~123 ka when *G. ruber* derived surface $\delta^{18}O_w$ abruptly increased, indicating a rapid increase in Sulu Sea surface salinity during the peak of MIS 5e (Figure 2c). This is approximately when Sarr et al. (2019) estimate the southern Sunda Shelf and Karimata Strait were inundated solely based on their estimated subsidence rates, suggesting those subsidence rates are reasonable. We also interpret the decrease in *G. ruber* derived surface $\delta^{18}O_w$ beginning at ~119 ka as evidence that the Karimata Strait closed again at that time, strengthening the connection between the South China Sea and Sulu Sea, and freshening the Sulu Sea surface. *G. ruber* derived surface $\delta^{18}O_w$ remained relatively constant from ~118–77 ka, the duration of MIS 5d–5a (118–72 ka), showing little to no evidence of the MIS 5d (117–108 ka) and 5b (92–86 ka) cold intervals (Figure 2c). The absence of a response to MIS 5d and 5b is likely the result of elevated Sulu Sea salinity during MIS 5a and 5c due to an open Karimata Strait and a freshened Sulu Sea surface during MIS 5d and 5b due to a closed Karimata Strait. Such opening and closing of the Karimata Strait would cancel out changes in global $\delta^{18}O_w$ and keep Sulu Sea surface *G. ruber* $\delta^{18}O_w$ relatively constant during MIS 5d to 5a. The Karimata Strait was certainly closed leading into MIS 4 at ~77 ka, freshening the Sulu Sea surface and likely reducing the amplitude of the MIS 5a to MIS 4 transition in the *G. ruber* surface $\delta^{18}O_w$ record compared to the *G. tumida* thermocline record. Low *G. ruber* derived surface $\delta^{18}O_w$ during MIS 3 from ~60 ka until the hiatus in the core at ~32 ka (Figure 2c) indicates the Karimata Strait remained closed for the duration of MIS 3.

4.2.3. Climatic Implications of Sunda Shelf Inundation History

Our Sulu Sea surface and thermocline reconstruction is the most direct record of Karimata Strait opening and closing and is unique in that it does not rely on drawing inferences from GMSL. Other foraminiferal $\delta^{18}O$, coral, and ice margin-based sea level records (Batchelor et al., 2019; Cutler et al., 2003; Linsley et al., 2010; Pico et al., 2017; Pico et al., 2017, 2017; Siddall et al., 2008; Spratt & Lisiecki, 2016) suggest the Karimata Strait was closed from the beginning of MIS 2 to the early Holocene and for the entirety of MIS 4 but could not conclusively demonstrate whether the strait was open or closed during MIS 3. By demonstrating that MIS 3 Sulu Sea *G. ruber* $\delta^{18}O_w$ was approximately equal to MIS 5a–5d $\delta^{18}O_w$ from ~60–32 ka, thus indicating the Karimata Strait was closed from ~60–32 ka (Figure 2c), our record fills that gap. Therefore, our reconstruction shows that the Karimata Strait was indeed closed for the entirety of the interval from approximately the beginning of MIS 4 to the early Holocene (~77–9.5 ka).

A closed Karimata Strait during MIS 3 and prior to the strait first opening at ~123 ka during MIS 5e impacts Indo-Pacific climate through two primary mechanisms. First, inundation of the Sunda Shelf promotes Indo-Pacific atmospheric convection and precipitation while reducing precipitation in the western Indian Ocean (Di Nezio et al., 2016; Pico et al., 2020). Our flooding history of the Karimata Strait shows that the shelf was never fully inundated during MIS 3 and caps maximum possible inundation and by extension, may relate to atmospheric convection and precipitation in the region during MIS 3. Using an ice sheet model and without taking into account Sunda Shelf subsidence, Pico et al. (2020) speculate that under maximum MIS 3 sea level nearly the entire Sunda

Shelf including the Karimata Strait was inundated, promoting atmospheric convection and precipitation in the region. Because our record only stipulates the Karimata Strait be closed, it cannot distinguish between a mostly inundated Sunda Shelf with a subaerial Karimata Strait and a largely exposed Sunda Shelf. Our results are therefore largely consistent with, but cannot corroborate the paleoclimatic conclusions of Pico et al. (2020) that a mostly inundated Sunda Shelf promoted atmospheric convection and precipitation in the Indo-Pacific during MIS 3. Second, modern southward flow through the Karimata Strait from the South China Sea forms a seasonal freshwater cap in the southern Makassar Strait that limits warm surface flow of the Indonesian Throughflow (ITF), the only low latitude connection between ocean basins (Gordon et al., 2003, 2011; Linsley et al., 2010). Our Karimata Strait flooding record suggests this cap could not have formed during the entirety of MIS 3 or prior to 125 ka, allowing for a shallower and warmer ITF. Radiogenic Nd, Sr, and Pb isotope records from the Timor Sea off the coast of Australia indicate the ITF was persistently strong during MIS 3 (Stumpf et al., 2015), supporting our interpretation the freshwater cap could not have formed during MIS 3. Conversely, modeling suggests that closing the Karimata Strait weakens the ITF as a whole (Di Nezio et al., 2016), so it is unclear precisely how this would interact with a lack of a freshwater cap.

4.2.4. Human and Faunal Migration Implications

Our record of the flooding history of the Karimata Strait during MIS 3 also offers insights into a critical period for modern human and megafaunal migration (Clarkson et al., 2017; de Bruyn et al., 2014; Husson et al., 2020; O'Connell et al., 2018; Teixeira et al., 2021). The earliest definitive evidence of modern humans on the island of Borneo can be dated to ~40 ka (O'Connell et al., 2018). We provide the most direct evidence that the Karimata Strait was exposed during the full duration of MIS 3 and could have served as a land bridge to facilitate land based human migration from Sumatra to Borneo. There is further evidence that modern humans reached the Sahul Shelf (between Australia and New Guinea) by ~40 ka and the islands between the Sunda and Sahul Shelves (Wallacea) by ~50–70 ka (Borregine et al., 2022; Kealy et al., 2018; O'Connell et al., 2018). Our data support the conclusion that these migrations were also likely facilitated by a Karimata Strait land bridge (Borregine et al., 2022; Kealy et al., 2018).

Borneo is a hotspot of global mammal diversity in part due to its episodic connection with the rest of the Sunda Shelf that allows inter-island migration during episodes of low sea level and divergent evolution under high sea level (de Bruyn et al., 2014). However, evidence suggests that not only sea level, but also climate regulated vegetation controls when inter-island migration occurred. By demonstrating the land bridge between Sumatra and Borneo existed for the duration of MIS 3, our record shows that terrestrial migration was possible between the two islands for the wide range of climate states throughout the interval spanning the beginning of MIS 4 to the early Holocene.

4.3. The Karimata Strait and Sea Level

4.3.1. Calculating Sea Level Using the Karimata Strait Flooding Record

We can use our record of opening and closing of the Karimata Strait in combination with the depth of the strait through time to constrain GMSL during MIS 3 and 5. During periods when the Karimata Strait was closed, we know that sea level must have been below the depth of the strait. In contrast, sea level must have been above the depth of the Karimata Strait when it was open. Whereas other $\delta^{18}O$ based sea level records rely on hydraulic modeling (Siddall et al., 2003) or assumptions about the relationship between $\delta^{18}O$ and global ice volume (Rohling et al., 2008; Siddall et al., 2008; Spratt & Lisiecki, 2016), our $\delta^{18}O$ based sea level record is unique in that it can be utilized to constrain sea level using a geologic feature, the Karimata Strat, that has a direct relationship to sea level.

Before we can estimate GMSL from the Karimata Strait, we must first account for several variables controlling strait depth through time. First, the modern topographic sill depth of the Karimata Strait is ~36 m (Figures 3a and 3b), however this depth cannot be used to estimate relative sea level using our inundation record because the effective depth of any strait is actually shallower than the topographic depth (Tan et al., 2013; Whitehead, 1998). Second, the entire Sunda Shelf including the Karimata Strait has been subsiding since at least the beginning of MIS 5 (Sarr et al., 2019). Third, we must further account for the difference between relative and eustatic sea level.

The effective depth of a strait is the depth at which flow is reduced to near zero and is always shallower than the topographic sill depth. Effective sill depth depends on the along channel pressure gradient, wind stress, tidal currents, and the fluid viscosity induced by ocean turbulence, including frictional interaction with the sea floor

and side-wall boundaries (Tan et al., 2013; Whitehead, 1998). Assuming a near linear relationship of frictional with along channel velocity, it is expected that modern Karimata Strait throughflow transport would be reduced to near zero with a sea level drop of >31 m and the modern effective depth of the Karimata Strait is therefore estimated to be 31 m (See Supplement for full explanation).

Geologic evidence suggests the Sunda Shelf and the Karimata Strait have been subsiding to the modern topographic depth of the Karimata Strait of 36 m at a relatively constant rate since at least the beginning of MIS 5 (Figure 3c) (Hanebuth et al., 2011; Sarr et al., 2019; Wong et al., 2003). As a result, when using the depth to place constraints on MIS 3 and MIS 5 GMSL we must use estimates of subsidence rates to correct for the shallower depth of the Karimata Strait in the past. Sedimentological estimates of Quaternary subsidence of the northern interior Sunda Shelf range from 0.13 to 0.27 mm/yr (Hanebuth et al., 2011; Wong et al., 2003). At Belitung Island on the western edge of the Karimata Strait (see Figures 1 and 3a), Sarr et al. (2019) use a combination of reef geomorphology, reef growth modeling, and seismic stratigraphy to estimate a subsidence rate of ∼0.25 ± 0.5 mm/yr. Subsidence rates appear to be relatively consistent across the shelf (Sarr et al., 2019). We choose to use the subsidence rate at Belitung Island estimated by Sarr et al. (2019) when constraining sea level as that is the most proximal estimate to the Karimata Strait.

To translate a Karimata Strait based estimate of relative sea level to GMSL, we must also account for GIA. We use the Creveling et al. (2017) model derived GIA correction for their site at the Huon Peninsula, Papua New Guinea. Their GIA correction for the Karimata Strait and almost the entire Indo-Pacific is the same as the Huon Peninsula at 80 ka (Creveling et al., 2017) and we assume this relationship holds true for the duration of our Sulu Sea reconstruction. The maximum correction for the Huon Peninsula is ∼−15 m (i.e., GMSL was 15 m lower than relative sea level at Huon Peninsula) at ∼11 ka, however the correction is equal to or below ∼−6 m for the intervals we estimate GMSL during MIS 3 and older. The correction is >0 m prior to ∼106 ka and reaches a maximum of ∼+2 m at ∼111 ka. Because the correction begins at ∼120 ka, we use a correction of +1.5 m, the approximate value from ∼120 to 111 ka, for 120–123 ka.

Our GMSL estimates must also take into account possible sedimentation and erosion modulating the depth of the Karimata Strait. We have already shown that the strait was mostly exposed from MIS 5e to the early Holocene and continuously exposed prior to MIS 5e. As a result, marine deposition could only have occurred during parts of MIS 5e, 5c, and 5a and the Holocene. Relatively high velocity flow through the Karimata Strait when it is open however, greatly limits deposition in the strait itself and downslope on the Sunda Shelf (Hanebuth et al., 2011; Hanebuth & Stattegger, 2003). This is demonstrated by the fact that opening of the strait in the early Holocene eroded downslope sediments that were deposited deeper on the Sunda Shelf when a closed strait prevented this higher velocity flow (Hanebuth & Stattegger, 2003). We therefore conclude that marine sediment deposition could not have played a large role in modulating the depth of the Karimata Strait. Furthermore, the lack of erodible sediments in the Karimata Strait limits the impact erosion could have on our sea level estimates as well. Hanebuth et al. (2011) do observe paleosols on the Sunda Shelf ranging in thickness from one to several meters that were deposited during periods of exposure. Limited sedimentological data from the Karimata Strait means it is unclear if these paleosols are or were ever present in the strait. If they were, they may also have been eroded at any point in time when the strait was inundated. To account for potential changes in Karimata Strait depth due to possible paleosol deposition and erosion as well as very limited sedimentation, we add ±3 m of uncertainty to our sea level estimates.

4.3.2. MIS 3 and 5 GMSL Estimates

Using the subsidence history of the Karimata Strait and its modern effective depth of 31 m, we are able to place upper bounds on possible GMSL during MIS 3 when our data indicate the strait was closed and sea level had to be below the effective depth of the strait. Conversely, our results place lower bounds on possible GMSL during MIS 5e, 5c, and 5a when the Karimata Strait appeared to have been open and sea level had to be above the depth of the strait (Figure 5). An open Karimata Strait from ∼123 to 119 ka during MIS 5e suggests minimum possible sea level was +1.3 ± 9 m at 123 ka and ∼0 ± 9 m at 119 ka (Figure 5). With an open Karimata Strait, minimum possible sea level during relatively warm MIS 5c was −3 ± 8 m at 108 ka at the beginning of the stage and −8 ± 8 m at the end of the stage. Similarly, an open Karimata Strait indicates that minimum possible sea level during warm MIS 5a was −11 ± 7 m at ∼86 ka and −12 ± 7 m at ∼77 ka (Figure 5). We constrain maximum allowable sea level during MIS 3 to −22 ± 6 m at ∼60 ka at the start of the interval and −29 ± 5 m at 32 ka, the end or our record (Figure 5).

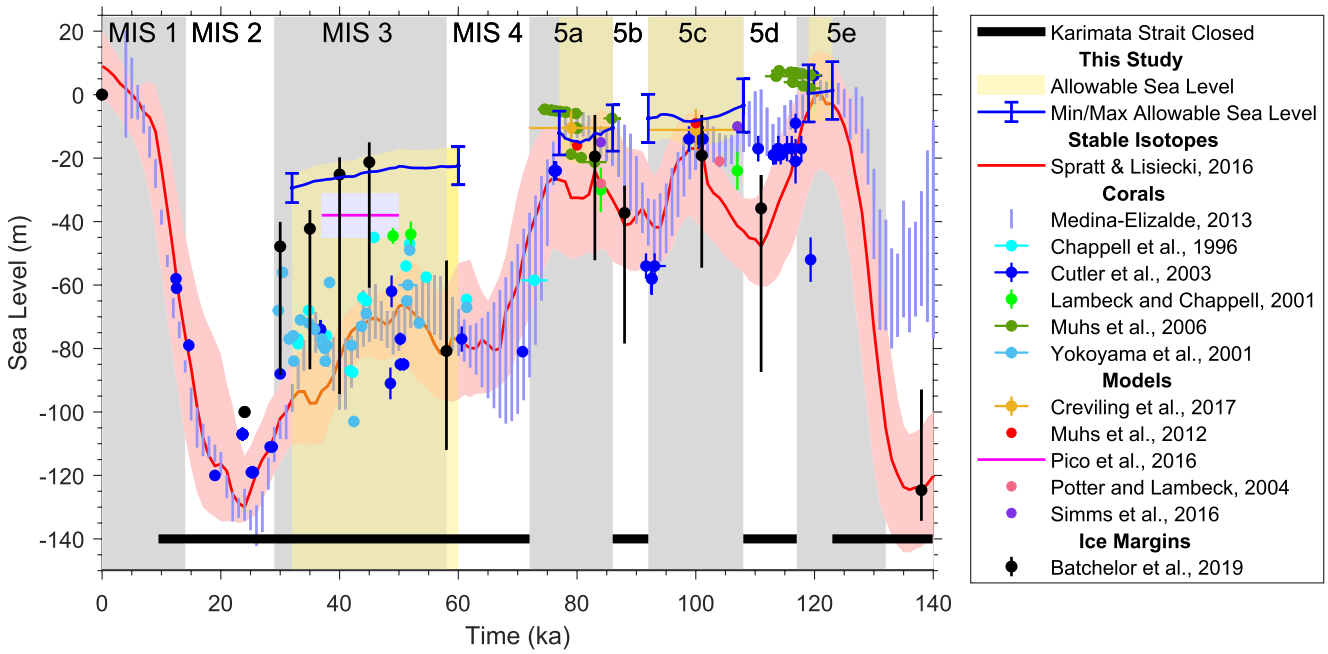

Figure 5. Our estimates of maximum allowable sea level during Marine Isotope Stage 3 (MIS 3) and minimum allowable sea level during MIS 5 compared to other sea level constraints. Blue bars for our study represent the Glacial Isostatic Adjustment (GIA) corrected effective depth of the Karimata Strait adjusted for the average subsidence rate. Uncertainty bars represent the GIA corrected (Creveling et al., 2017) effective depth of the Karimata Strait adjusted for the maximum and minimum subsidence (Sarr et al., 2019) rate along with a ±3 m uncertainty to account for sedimentation. Our sea level constraints view any sea level within the yellow shading as equally likely because our constraints only stipulate sea level must have been below the effective depth of the Karimata Strait during MIS 3 and above the depth of the strait during MIS 5a, 5c, and 5e. Thick black bars near the bottom of the plot represent periods when we argue the Karimata Strait was closed. Evidence for a closed Karimata Strait during MIS 3, MIS 5b, 5d, and early 5e and before come from this study. It is possible the Karimata Strait was also closed during late MIS 5a and early and late MIS5 5c, but the evidence in our reconstruction is unclear. Evidence for a closed Karimata Strait during early MIS 1 and MIS 2 comes from Linsley et al. (2010) and Rosenthal et al. (2003a). A closed Karimata Strait during MIS 4 can be inferred from any of the other sea level records covering that interval shown in this figure.

4.3.3. Comparison to Other Sea Level Records

Our estimate of MIS 5e sea level conforms with other evidence that MIS 5e sea level was at or above modern sea level (Figure 5) (Dutton et al., 2015; Medina-Elizalde, 2013; Muhs et al., 2006) and further supports a sea level elevation maximum later during MIS 5e beginning around 123 ka (Medina-Elizalde, 2013; Muhs et al., 2006). Previous estimates of MIS 5a and 5c sea level appear to fall into two main groups, those estimating −20 m relative to today or lower and those estimates that suggest sea level was −15 m relative to today or higher (Figure 5). Our estimates of minimum allowable MIS 5a and 5c sea level favor the higher group of sea level reconstructions, plotting above the mean values and in the top of the error window for the Batchelor et al. (2019) ice margin and Spratt and Lisiecki (2016) $\delta^{18}O$ reconstructions (Figure 5). Our MIS 5c estimates are in good agreement with several sea level records based on corals (Cutler et al., 2003), GIA modeling based on marine terraces and shoreline and coastal indicators (Creveling et al., 2017; Muhs et al., 2012; Simms et al., 2015) and statistical coral compilations (Medina-Elizalde, 2013) that plot just below our mean estimates and are encompassed within our error window. During MIS 5a, our sea level estimates are in even better agreement with those records (Creveling et al., 2017; Cutler et al., 2003; Muhs et al., 2006, 2012; Simms et al., 2015). We do note that most other sea level records indicate peaks in MIS 5a and 5c sea level shorter in duration than our record (Creveling et al., 2017; Cutler et al., 2003; Muhs et al., 2006, 2012; Potter & Lambeck, 2004; Simms et al., 2015; Spratt & Lisiecki, 2016). It is possible that shorter term variability in our *G. ruber* $\delta^{18}O_w$ data obscures lower frequency increases in $\delta^{18}O_w$ during MIS 5a and 5c and the Karimata Strait was only open during a portion of those two periods and as such, our estimates may only apply to the intervals of maximum sea level during MIS 5a and 5c.

Our Sulu Sea reconstructions and Karimata Strait based GMSL record address the MIS 3 sea level controversy in two ways. The first is by directly constraining GMSL using the effective depth of the Karimata Strait through time and our new inundation history. Because our Karimata Strait inundation history only allows us to constrain maximum possible GMSL during MIS 3, but does not show when or if sea level ever reached the maximum

allowed by our record, we interpret any sea level record that plots below our maximum constrained sea level as in agreement with our record. Our estimate of maximum possible sea level during MIS 3 is relatively shallow and is therefore consistent with both the lower coral and $\delta^{18}O$ based MIS 3 sea level estimates (Chappell et al., 1996; Cutler et al., 2003; Spratt & Lisiecki, 2016; Yokoyama et al., 2001) and the higher GIA modeling, shoreline, and ice margin-based estimates (Batchelor et al., 2019; Dalton et al., 2022; Pico et al., 2016, 2017).

The second way our Sulu Sea reconstructions address the MIS 3 controversy is in regard to comparisons between GIA modeling, shoreline, and ice margin-based GMSL estimates and interpretations of the GMSL contributions to foraminiferal $\delta^{18}O$ records (see Dalton et al., 2022). If higher estimates of maximum MIS 3 sea level of approximately −40 m are correct (Batchelor et al., 2019; Dalton et al., 2022; Pico et al., 2016, 2017), as discussed in Dalton et al. (2022), there is a clear disconnect between those paleo-records and interpretations of the sea level components of foraminiferal $\delta^{18}O$ reconstructions (Siddall et al., 2008; Spratt & Lisiecki, 2016). It has been speculated that the similarities between low Sulu Sea *G. ruber* surface $\delta^{18}O$ during MIS 3 and high sea level estimates during that period are possibly the result of the isolated nature of the Sulu Sea and that the Sulu Sea $\delta^{18}O$ record could be one of the few $\delta^{18}O$ records that does not have confounding influences overprinting the sea level component (Linsley, 1996). If this were the case, Sulu Sea *G. ruber* surface $\delta^{18}O$ would directly support shallow GMSL estimates during MIS 3. However, we demonstrate that thermocline $\delta^{18}O_w$ in the Sulu Sea more closely scales to the LR04 benthic stack with higher $\delta^{18}O_w$ during MIS 3 than MIS 5, indicating that low surface $\delta^{18}O$ and $\delta^{18}O_w$ in the Sulu Sea during MIS 3 are the result of local surface freshening due to circulation changes. Therefore, Sulu Sea *G. ruber* surface $\delta^{18}O$ cannot be used to resolve the potential disconnect between higher MIS 3 GMSL estimates and interpretations of the sea level component of $\delta^{18}O$ records. Though because global $\delta^{18}O_w$ and sea level are not perfectly proportional, our record does not necessarily favor lower MIS 3 sea level estimates or suggest an explanation for the apparent disconnect between higher MIS 3 GMSL estimates and interpretations of the sea level component of $\delta^{18}O$ records doesn't exist.

5. Conclusions

Inundation and exposure of the Karimata Strait in Indonesia due to rising and falling sea level controls Sulu Sea surface salinity by regulating whether a portion of relatively fresh South China Sea outflow can flow through the strait or is redirected through the Sulu Sea. We take a novel approach to constraining sea level utilizing $\delta^{18}O$ and Mg/Ca analyses of Sulu Sea surface-dwelling *G. ruber* and thermocline-dwelling *G. tumida* to show the Sulu Sea surface was relatively fresh and the Karimata Strait was subaerially exposed during MIS 3 and the Sulu Sea surface was relatively salty and the Karimata Strait was inundated during portions of MIS 5a, 5c, and 5e.

Sea level induced exposure and inundation of the Sunda Shelf during MIS 3, 4, and 5 likely played an important role in atmospheric convection (Di Nezio et al., 2016; Pico et al., 2020) as well as the temperature profile of the ITF (Gordon et al., 2011). The earliest evidence of modern humans on the island of Borneo is dated to ∼40 ka, the middle of MIS 3 (Borregine et al., 2022; Clarkson et al., 2017; de Bruyn et al., 2014; Husson et al., 2020; Kealy et al., 2018; O'Connell et al., 2018; Teixeira et al., 2021) when our results show an exposed Sunda Shelf and Karimata Strait would have facilitated migration from the mainland.

Our record demonstrates a method for using geochemical proxies to estimate GMSL by tying circulation changes to the physical depth of the Karimata Strait through time. Using the subsidence rate of the Sunda Shelf (Sarr et al., 2019) and correcting for GIA, we estimated the effective depth of the Karimata Strait through time and were able to constrain minimum possible GMSL from ∼123 to 119 ka during MIS 5e to +1 ± 9 m to 0 ± 9 m relative to modern. We constrain minimum possible GMSL to −3 ± 8 m and −8 ± 8 m at the beginning and end of MIS 5a and −11 ± 7 m and −12 ± 7 m relative to modern sea level at the beginning and end of MIS 5a, respectively. Our results show that lower than expected $\delta^{18}O_w$ values in the Sulu Sea surface were not predominantly driven by the global ice volume effects on $\delta^{18}O_w$ and the sheltered bathymetry of the Sulu Sea, but were lowered when the Karimata Strait was closed and there was enhanced delivery of relatively fresh water to the Sulu Sea surface from the South China Sea. We are able to constrain maximum possible GMSL at the beginning of MIS 3 to −22 ± 6 m below modern and at the end of MIS 3 to −29 ± 5 m. These estimates are consistent with both lower sea level estimates based on coral and $\delta^{18}O$ (Chappell et al., 1996; Cutler et al., 2003; Spratt & Lisiecki, 2016; Yokoyama et al., 2001) and higher sea level estimates based on GIA modeling, shoreline, and ice margins (Batchelor et al., 2019; Pico et al., 2016, 2017; Siddall et al., 2008). Our record does support higher

global $\delta^{18}O_w$ during MIS 3 than MIS 5, but this does not rule out higher sea level estimates during MIS 3 as global $\delta^{18}O_w$ and sea level are not perfectly proportional.

Conflict of Interest

The authors declare no conflicts of interest relevant to this study.

Data Availability Statement

Previously published *G. ruber* and *G. tumida* $\delta^{18}O$ and Mg/Ca data in the main text and Figure S3 in Supporting Information S1 (i.e., Dannenmann et al., 2003; Oppo et al., 2003b; Rosenthal et al., 2003a; Weiss et al., 2021b) are available on the NOAA National Centers For Environmental Information (NCEI) web page at Oppo et al. (2003a), Rosenthal et al. (2003b), and Weiss et al. (2021a). All *G. ruber* Mg/Ca and *G. tumida* $\delta^{18}O$ and Mg/Ca newly published in this manuscript are available in the NOAA National Centers for Environmental Information (NCEI) at Weiss et al. (2022). Data from Lisiecki and Raymo (2005) are available at https://lorraine-lisiecki.com/stack.html. Elevation data used to generate Figures 3a and 3b and Figures S1 and S2 in Supporting Information S1 are available at NOAA National Geophysical Data Center. (2009). Carolin et al. (2016b) speleothem data are available on the NOAA NCEI web page at Carolin et al. (2016a). Cheng et al. (2016), Spratt and Lisiecki (2016), Pico et al. (2016), Creveling et al. (2017), and Cutler et al. (2003) data are available in the papers or in their supporting information. Potter and Lambeck (2004), Muhs et al. (2012), Simms et al. (2015), and Lambeck and Chappell (2001) sea level highstands were estimated from figures in the papers. Data from Medina-Elizalde (2013) data are available in their supporting information which also includes compiled data from Chappell et al. (1996), Muhs et al. (2006), and Yokoyama et al. (2001) with recalculated depths and recalibrated ages plotted here. Batchelor et al. (2019) ice volume data are available at Batchelor et al. (2021) and sea level data in their paper and their supporting information.

Acknowledgments
This work was supported by National Science Foundation (Grant No. OCE-1736602) to BKL and a Lamont-Doherty Earth Observatory Climate Center grant to BKL and TLW. We also acknowledge earlier NSF awards to BKL (Grant No. OCE-9710156) and YR (Grant No. OCE-9987060). The authors thank Dr. Jerry McManus for assistance with data interpretation. We also thank Dr. Wei Huang and Dr. Ann Olsson for their assistance in analyzing samples.

References

Anand, P., Elderfield, H., & Conte, M. H. (2003). Calibration of Mg/Ca thermometry in planktonic foraminifera from a sediment trap time series. *Paleoceanography*, *18*(2), 28. https://doi.org/10.1029/2002PA000846

Arbuszewski, J., de Menocal, P., Kaplan, A., & Farmer, E. C. (2010). On the fidelity of shell-derived $\delta^{18}O_{seawater}$ estimates. *Earth and Planetary Science Letters*, *300*(3–4), 185–196. https://doi.org/10.1016/j.epsl.2010.10.035

Barker, S., Greaves, M., & Elderfield, H. (2003). A study of cleaning procedures used for foraminiferal Mg/Ca paleothermometry. *Geochemistry, Geophysics, Geosystems*, *4*(9), 8407. https://doi.org/10.1029/2003GC000559

Batchelor, C., Krapp, M., Manica, A., & Murton, D., (2021). The configuration of northern hemisphere ice sheets through the quaternary [Dataset]. Open Science Framework. https://doi.org/10.17605/OSF.IO/7JEN3

Batchelor, C. L., Margold, M., Krapp, M., Murton, D. K., Dalton, A. S., Gibbard, P. L., et al. (2019). The configuration of Northern Hemisphere ice sheets through the Quaternary. *Nature Communications*, *10*(1), 3713. https://doi.org/10.1038/s41467-019-11601-2

Bemis, B. E., Spero, H. J., Bijma, J., & Lea, D. W. (1998). Reevaluation of the oxygen isotopic composition of planktonic foraminifera: Experimental results and revised paleotemperature equations. *Paleoceanography*, *13*(2), 150–160. https://doi.org/10.1029/98PA00070

Blunier, T., Chappellaz, J., Schwander, J., Dällenbach, A., Stauffer, B., Stocker, T. F., et al. (1998). Asynchrony of Antarctic and Greenland climate change during the last glacial period. *Nature*, *394*(6695), 739–743. https://doi.org/10.1038/29447

Borreggine, M., Powell, E., Pico, T., Mitrovica, J. X., Meadow, R., & Tryon, C. (2022). Not a bathtub: A consideration of sea-level physics for archaeological models of human migration. *Journal of Archaeological Science*, *137*, 105507. https://doi.org/10.1016/j.jas.2021.105507

Carolin, S. A., Cobb, K. M., Lynch-Stieglitz, J., Moerman, J. W., Partin, J. W., Lejau, S., et al. (2016a). NOAA/WDS Paleoclimatology - Borneo 160,000 year stalagmite oxygen isotope data [Dataset]. NOAA National Centers for Environmental Information (NCEI). https://doi.org/10.25921/rxkn-e268

Carolin, S. A., Cobb, K. M., Lynch-Stieglitz, J., Moerman, J. W., Partin, J. W., Lejau, S., et al. (2016b). Northern Borneo stalagmite records reveal West Pacific hydroclimate across MIS 5 and 6. *Earth and Planetary Science Letters*, *439*, 182–193. https://doi.org/10.1016/j.epsl.2016.01.028

Chappell, J. (2002). Sea level changes forced ice breakouts in the last glacial cycle: New results from coral terraces. *Quaternary Science Reviews*, *21*(10), 1229–1240. https://doi.org/10.1016/S0277-3791(01)00141-X

Chappell, J., Omura, A., Esat, T., McCulloch, M., Pandolfi, J., Ota, Y., & Pillans, B. (1996). Reconciliation of late Quaternary sea levels derived from coral terraces at Huon Peninsula with deep sea oxygen isotope records. *Earth and Planetary Science Letters*, *141*(1–4), 227–236. https://doi.org/10.1016/0012-821X(96)00062-3

Cheng, H., Edwards, R. L., Sinha, A., Spötl, C., Yi, L., Chen, S., et al. (2016). The Asian monsoon over the past 640, 000 years and ice age terminations. *Nature*, *534*(7609), 640–646. https://doi.org/10.1038/nature18591

Clarkson, C., Jacobs, Z., Marwick, B., Fullagar, R., Wallis, L., Smith, M., et al. (2017). Human occupation of northern Australia by 65, 000 years ago. *Nature*, *547*(7663), 306–310. https://doi.org/10.1038/nature22968

Creveling, J. R., Mitrovica, J. X., Clark, P. U., Waelbroeck, C., & Pico, T. (2017). Predicted bounds on peak global mean sea level during marine isotope stages 5a and 5c. *Quaternary Science Reviews*, *163*, 193–208. https://doi.org/10.1016/j.quascirev.2017.03.003

Cutler, K. B., Edwards, R. L., Taylor, F. W., Cheng, H., Adkins, J., Gallup, C. D., et al. (2003). Rapid sea-level fall and deep-ocean temperature change since the last interglacial period. *Earth and Planetary Science Letters*, *206*(3–4), 253–271. https://doi.org/10.1016/S0012-821X(02)01107-X

Dalton, A. S., Finkelstein, S. A., Forman, S. L., Barnett, P. J., Pico, T., & Mitrovica, J. X. (2019). Was the Laurentide Ice Sheet significantly reduced during Marine Isotope Stage 3? *Geology*, *47*(2), 111–114. https://doi.org/10.1130/G45335.1

Dalton, A. S., Pico, T., Gowan, E. J., Clague, J. J., Forman, S. L., McMartin, I., et al. (2022). The marine $\delta^{18}O$ record overestimates continental ice volume during Marine Isotope Stage 3. *Global and Planetary Change*, *212*, 103814. https://doi.org/10.1016/j.gloplacha.2022.103814

Dannenmann, S., Linsley, B. K., Oppo, D. W., Rosenthal, Y., & Beaufort, L. (2003). East Asian monsoon forcing of suborbital variability in the Sulu Sea during Marine Isotope Stage 3: Link to Northern Hemisphere climate. *Geochemistry, Geophysics, Geosystems*, *4*(1), 1–13. https://doi.org/10.1029/2002GC000390

de Bruyn, M., Stelbrink, B., Morley, R. J., Hall, R., Carvalho, G. R., Cannon, C. H., et al. (2014). Borneo and Indochina are major evolutionary hotspots for Southeast Asian biodiversity. *Systematic Biology*, *63*(6), 879–901. https://doi.org/10.1093/sysbio/syu047

de Garidel-Thoron, T., Beaufort, L., Linsley, B. K., & Dannenmann, S. (2001). Millennial-scale dynamics of the East Asian winter monsoon during the last 200, 000 years. *Paleoceanography*, *16*(5), 491–502. https://doi.org/10.1029/2000PA000557

Dekens, P. S., Lea, D. W., Pak, D. K., & Spero, H. J. (2002). Core top calibration of Mg/Ca in tropical foraminifera: Refining paleotemperature estimation. *Geochemistry, Geophysics, Geosystems*, *3*(4), 1–29. https://doi.org/10.1029/2001GC000200

Di Nezio, P. N., Timmermann, A., Tierney, J. E., Jin, F., Otto-Bliesner, B., Rosenbloom, N., et al. (2016). The climate response of the Indo-Pacific warm pool to glacial sea level. *Paleoceanography*, *31*(6), 866–894. https://doi.org/10.1002/2015PA002890

Dutton, A., Carlson, A. E., Long, A. J., Milne, G. A., Clark, P. U., DeConto, R., et al. (2015). Sea-level rise due to polar ice-sheet mass loss during past warm periods. *Science*, *349*(6244), aaa4019. https://doi.org/10.1126/science.aaa4019

Gordon, A., & Villanoy, C. (2011). The oceanography of the Philippine archipelago: Introduction to the special issue. *Oceanography*, *24*(01), 13. https://doi.org/10.5670/oceanog.2011.13

Gordon, A. L., Giulivi, C. F., & Ilahude, A. G. (2003). Deep topographic barriers within the Indonesian seas. *Deep Sea Research Part II: Topical Studies in Oceanography*, *50*(12–13), 2205–2228. https://doi.org/10.1016/S0967-0645(03)00053-5

Gordon, A. L., Huber, B. A., Metzger, E. J., Susanto, R. D., Hurlburt, H. E., & Adi, T. R. (2012). South China Sea throughflow impact on the Indonesian Throughflow. *Geophysical Research Letters*, *39*(11), L11602. https://doi.org/10.1029/2012GL052021

Gordon, A. L., Tessler, Z. D., & Villanoy, C. (2011). Dual overflows into the deep Sulu Sea. *Geophysical Research Letters*, *38*(18), L18606. https://doi.org/10.1029/2011GL048878

Gowan, E. J., Zhang, X., Khosravi, S., Rovere, A., Stocchi, P., Hughes, A. L. C., et al. (2021). A new global ice sheet reconstruction for the past 80 000 years. *Nature Communications*, *12*(1), 1199. https://doi.org/10.1038/s41467-021-21469-w

Gray, W. R., & Evans, D. (2019). Nonthermal influences on Mg/Ca in planktonic foraminifera: A review of culture studies and application to the Last Glacial Maximum. *Paleoceanography and Paleoclimatology*, *34*(3), 306–315. https://doi.org/10.1029/2018PA003517

Hanebuth, T. J. J., Saito, Y., Tanabe, S., Vu, Q. L., & Ngo, Q. T. (2006). Sea levels during late Marine Isotope Stage 3 (or older?) reported from the Red River delta (northern Vietnam) and adjacent regions. *Quaternary International*, *145*(146), 119–134. https://doi.org/10.1016/j.quaint.2005.07.008

Hanebuth, T. J. J., & Stattegger, K. (2003). The Stratigraphic evolution of the Sunda Shelf during the past fifty thousand years. In F. H. Sidi, D. Nummedal, P. Imbert, H. Darman, & H. W. Posamentier (Eds.), *Tropical deltas of southeast asia—sedimentology, stratigraphy, and petroleum geology* (Vol. 76, pp. 189–200). SEPM Society for Sedimentary Geology. https://doi.org/10.2110/pec.03.76.0189

Hanebuth, T. J. J., Voris, H. K., Yokoyama, Y., Saito, Y., & Okuno, J. (2011). Formation and fate of sedimentary depocentres on Southeast Asia's Sunda Shelf over the past sea-level cycle and biogeographic implications. *Earth-Science Reviews*, *104*(1–3), 92–110. https://doi.org/10.1016/j.earscirev.2010.09.006

Hollstein, M., Mohtadi, M., Rosenthal, Y., Moffa Sanchez, P., Oppo, D., Martínez Méndez, G., et al. (2017). Stable oxygen isotopes and Mg/Ca in planktic foraminifera from modern surface sediments of the Western Pacific Warm Pool: Implications for thermocline reconstructions. *Paleoceanography*, *32*(11), 1174–1194. https://doi.org/10.1002/2017PA003122

Husson, L., Boucher, F. C., Sarr, A., Sepulchre, P., & Cahyarini, S. Y. (2020). Evidence of Sundaland's subsidence requires revisiting its biogeography. *Journal of Biogeography*, *47*(4), 843–853. https://doi.org/10.1111/jbi.13762

Kealy, S., Louys, J., & O'Connor, S. (2018). Least-cost pathway models indicate northern human dispersal from Sunda to Sahul. *Journal of Human Evolution*, *125*, 59–70. https://doi.org/10.1016/j.jhevol.2018.10.003

Lambeck, K., & Chappell, J. (2001). Sea level change through the last glacial cycle. *Science*, *292*(5517), 679–686. https://doi.org/10.1126/science.1059549

Linsley, B. K. (1996). Oxygen-isotope record of sea level and climate variations in the Sulu Sea over the past 150, 000 years. *Nature*, *380*(6571), 234–237. https://doi.org/10.1038/380234a0

Linsley, B. K., Rosenthal, Y., & Oppo, D. W. (2010). Holocene evolution of the Indonesian Throughflow and the Western Pacific Warm Pool. *Nature Geoscience*, *3*(8), 578–583. https://doi.org/10.1038/ngeo920

Lisiecki, L. E., & Raymo, M. E. (2005). A Pliocene-Pleistocene stack of 57 globally distributed benthic $\delta^{18}O$ records. *Paleoceanography*, *20*(1), PA1003. https://doi.org/10.1029/2004PA001071

Mathien-Blard, E., & Bassinot, F. (2009). Salinity bias on the foraminifera Mg/Ca thermometry: Correction procedure and implications for past ocean hydrographic reconstructions. *Geochemistry, Geophysics, Geosystems*, *10*(12), Q12011. https://doi.org/10.1029/2008GC002353

Medina-Elizalde, M. (2013). A global compilation of coral sea-level benchmarks: Implications and new challenges. *Earth and Planetary Science Letters*, *362*, 310–318. https://doi.org/10.1016/j.epsl.2012.12.001

Miao, Q., Thunell, R. C., & Anderson, D. M. (1994). Glacial-Holocene carbonate dissolution and sea surface temperatures in the south China and Sulu seas. *Paleoceanography*, *9*(2), 269–290. https://doi.org/10.1029/93PA02830

Mohtadi, M., Prange, M., Oppo, D. W., De Pol-Holz, R., Merkel, U., Zhang, X., et al. (2014). North Atlantic forcing of tropical Indian Ocean climate. *Nature*, *509*(7498), 76–80. https://doi.org/10.1038/nature13196

Muhs, D. R., Simmons, K. R., Kennedy, G. L., Ludwig, K. R., & Groves, L. T. (2006). A cool eastern Pacific Ocean at the close of the Last Interglacial complex. *Quaternary Science Reviews*, *25*(3–4), 235–262. https://doi.org/10.1016/j.quascirev.2005.03.014

Muhs, D. R., Simmons, K. R., Schumann, R. R., Groves, L. T., Mitrovica, J. X., & Laurel, D. (2012). Sea-level history during the Last Interglacial complex on San Nicolas Island, California: Implications for glacial isostatic adjustment processes, paleozoogeography and tectonics. *Quaternary Science Reviews*, *37*, 1–25. https://doi.org/10.1016/j.quascirev.2012.01.010

NOAA National Geophysical Data Center. (2009). ETOPO1 1 arc-minute global relief model [Dataset]. NOAA National Centers for Environmental Information. https://doi.org/10.7289/V5C8276M Accessed 2/2021.

O'Connell, J. F., Allen, J., Williams, M. A. J., Williams, A. N., Turney, C. S. M., Spooner, N. A., et al. (2018). When did *Homo sapiens* first reach Southeast Asia and Sahul? *Proceedings of the National Academy of Sciences*, *115*(34), 8482–8490. https://doi.org/10.1073/pnas.1808385115

Oppo, D. W., Linsley, B. K., Rosenthal, Y., Dannenmann, S., & Beaufort, L. (2003a). NOAA/WDS Paleoclimatology - Oppo et al. 2003 Sulu Sea core MD97-2141 foraminiferal oxygen isotope data [Dataset]. NOAA National Centers for Environmental Information (NCEI). https://doi.org/10.25921/qqqx-kt90

Oppo, D. W., Linsley, B. K., Rosenthal, Y., Dannenmann, S., & Beaufort, L. (2003b). Orbital and suborbital climate variability in the Sulu Sea, western tropical Pacific. *Geochemistry, Geophysics, Geosystems*, *4*(1), 1–20. https://doi.org/10.1029/2001GC000260

Pico, T., Creveling, J. R., & Mitrovica, J. X. (2017). Sea-level records from the U.S. Mid-atlantic constrain Laurentide Ice Sheet extent during Marine Isotope Stage 3. *Nature Communications*, *8*(1), 15612. https://doi.org/10.1038/ncomms15612

Pico, T., McGee, D., Russell, J., & Mitrovica, J. X. (2020). Recent constraints on MIS 3 sea level support role of continental shelf exposure as a control on Indo-Pacific hydroclimate. *Paleoceanography and Paleoclimatology*, *35*(8). https://doi.org/10.1029/2020PA003998

Pico, T., Mitrovica, J. X., Ferrier, K. L., & Braun, J. (2016). Global ice volume during MIS 3 inferred from a sea-level analysis of sedimentary core records in the Yellow River Delta. *Quaternary Science Reviews*, *152*, 72–79. https://doi.org/10.1016/j.quascirev.2016.09.012

Potter, E.-K., & Lambeck, K. (2004). Reconciliation of sea-level observations in the Western North Atlantic during the last glacial cycle. *Earth and Planetary Science Letters*, *217*(1–2), 171–181. https://doi.org/10.1016/S0012-821X(03)00587-9

Rohling, E. J., Grant, K., Hemleben, C., Kucera, M., Roberts, A. P., Schmeltzer, I., et al. (2008). New constraints on the timing of sea level fluctuations during early to middle Marine Isotope Stage 3. *Paleoceanography*, *23*(3), PA3219. https://doi.org/10.1029/2008PA001617

Rosenthal, Y., & Lohmann, G. P. (2002). Accurate estimation of sea surface temperatures using dissolution-corrected calibrations for Mg/Ca paleothermometry. *Paleoceanography*, *17*(3), 1044. https://doi.org/10.1029/2001PA000749

Rosenthal, Y., Oppo, D. W., & Linsley, B. K. (2003a). The amplitude and phasing of climate change during the last deglaciation in the Sulu Sea, Western equatorial Pacific. *Geophysical Research Letters*, *30*(8), 11. https://doi.org/10.1029/2002GL016612

Rosenthal, Y., Oppo, D. W., & Linsley, B. K. (2003b). NOAA/WDS Paleoclimatology - Sulu Sea core MD97-2141 oxygen isotope and Mg/Ca data [Dataset]. NOAA National Centers for Environmental Information (NCEI). https://doi.org/10.25921/hnbh-q983

Ryan, W. B. F., Carbotte, S. M., Coplan, J. O., O'Hara, S., Melkonian, A., Arko, R., et al. (2009). Global Multi-resolution topography synthesis. *Geochemistry, Geophysics, Geosystems*, *10*(3), Q03014. https://doi.org/10.1029/2008GC002332

Sarr, A.-C., Husson, L., Sepulchre, P., Pastier, A.-M., Pedoja, K., Elliot, M., et al. (2019). Subsiding Sundaland. *Geology*, *47*(2), 119–122. https://doi.org/10.1130/G45629.1

Schmidt, M. W., Spero, H. J., & Lea, D. W. (2004). Links between salinity variation in the Caribbean and North Atlantic thermohaline circulation. *Nature*, *428*(6979), 160–163. https://doi.org/10.1038/nature02346

Siddall, M., Rohling, E. J., Almogi-Labin, A., Hemleben, C., Meischner, D., Schmelzer, I., & Smeed, D. A. (2003). Sea-level fluctuations during the last glacial cycle. *Nature*, *423*(6942), 853–858. https://doi.org/10.1038/nature01690

Siddall, M., Rohling, E. J., Thompson, W. G., & Waelbroeck, C. (2008). Marine Isotope Stage 3 sea level fluctuations: Data synthesis and new outlook. *Reviews of Geophysics*, *46*(4), RG4003. https://doi.org/10.1029/2007RG000226

Simms, A. R., Rouby, H., & Lambeck, K. (2015). Marine terraces and rates of vertical tectonic motion: The importance of glacio-isostatic adjustment along the Pacific coast of central North America. *The Geological Society of America Bulletin*, *1*, B31299. https://doi.org/10.1130/B31299.1

Spratt, R. M., & Lisiecki, L. E. (2016). A Late Pleistocene sea level stack. *Climate of the Past*, *12*(4), 1079–1092. https://doi.org/10.5194/cp-12-1079-2016

Stumpf, R., Kraft, S., Frank, M., Haley, B., Holbourn, A., & Kuhnt, W. (2015). Persistently strong Indonesian Throughflow during Marine Isotope Stage 3: Evidence from radiogenic isotopes. *Quaternary Science Reviews*, *112*, 197–206. https://doi.org/10.1016/j.quascirev.2015.01.029

Tan, S., Pratt, L. J., Yuan, D., Li, X., Wang, Z., Li, Y., et al. (2020). Hydraulics and mixing of the deep overflow in the lifamatola Passage of the Indonesian Seas. *Journal of Physical Oceanography*, *50*(9), 2797–2814. https://doi.org/10.1175/JPO-D-19-0326.1

Tan, S., Wang, Z., Wang, C., & Lan, S. (2013). Flow fluctuations and flow friction characteristics of vertical narrow rectangular channel under rolling motion conditions. *Experimental Thermal and Fluid Science*, *50*, 69–78. https://doi.org/10.1016/j.expthermflusci.2013.05.006

Teixeira, J. C., Jacobs, G. S., Stringer, C., Tuke, J., Hudjashov, G., Purnomo, G. A., et al. (2021). Widespread Denisovan ancestry in Island Southeast Asia but no evidence of substantial super-archaic hominin admixture. *Nature Ecology and Evolution*, *5*(5), 616–624. https://doi.org/10.1038/s41559-021-01408-0

The NOAA Technical Memorandum, Amante, C., & Eakins, B. W. (2009). *ETOPO1 1 arc-minute global Relief model: Procedures, data sources and analysis*. NOAA Technical Memorandum NESDIS NGDC-24. https://doi.org/10.7289/V5C8276M

Thompson, W. G. (2005). Open-system coral ages reveal persistent suborbital sea-level cycles. *Science*, *308*(5720), 401–404. https://doi.org/10.1126/science.1104035

Thompson, W. G., & Goldstein, S. L. (2006). A radiometric calibration of the SPECMAP timescale. *Quaternary Science Reviews*, *25*(23–24), 3207–3215. https://doi.org/10.1016/j.quascirev.2006.02.007

Wang, Y., Xu, T., Li, S., Susanto, R. D., Agustiadi, T., Trenggono, M., et al. (2019). Seasonal variation of water transport through the Karimata Strait. *Acta Oceanologica Sinica*, *38*(4), 47–57. https://doi.org/10.1007/s13131-018-1224-2

Weiss, T. L., Linsley, B. K., & Gordon, A. L. (2021a). NOAA/WDS Paleoclimatology - Sulu Sea core MD97-2141 Termination I *Globorotalia tumida* $\delta^{18}O$ and Mg/Ca data [Dataset]. NOAA National Centers for Environmental Information (NCEI). https://doi.org/10.25921/qt77-bv09

Weiss, T. L., Linsley, B. K., & Gordon, A. L. (2021b). Pacific North Equatorial Current bifurcation latitude and Kuroshio Current shifts since the Last Glacial Maximum inferred from a Sulu Sea thermocline reconstruction. *Quaternary Science Reviews*, *264*, 106999. https://doi.org/10.1016/j.quascirev.2021.106999

Weiss, T. L., Linsley, B. K., Gordon, A. L., Rosenthal, Y., & Dannenmann-Di Palma, S. (2022). NOAA/WDS Paleoclimatology – Sulu Sea core MD97-2141 *Globorotalia tumida* $\delta^{18}O$ and Mg/Ca data spanning marine isotope stages 3-5 [Dataset]. NOAA National Centers for Environmental Information (NCEI). https://doi.org/10.25921/b285-4433

Whitehead, J. A. (1998). Topographic control of oceanic flows in deep passages and straits. *Reviews of Geophysics*, *18*(3), 423–440. https://doi.org/10.1029/98rg01014

Wong, H. K., Ludmann, T., Haft, C., & Paulsen, A.-M. (2003). Quaternary sedimentation in the Molengraaff paleo-delta, northern Sunda-Shelf (southern South China Sea). In *Tropical deltas in Southeast Asia—Sedimentology, Stratigraphy, and Petroleum Geology* (Vol. 76, pp. 201–216). https://doi.org/10.2110/pec.03.76.0201

Xu, T. F., Wei, Z. X., Susanto, R. D., Li, S. J., Wang, Y. G., Wang, Y., et al. (2021). Observed water exchange between the south China Sea and Java Sea through Karimata Strait. *Journal of Geophysical Research: Oceans*, *126*(2). https://doi.org/10.1029/2020JC016608

Yokoyama, Y., Esat, T. M., & Lambeck, K. (2001). Coupled climate and sea-level changes deduced from Huon Peninsula coral terraces of the last ice age. *Earth and Planetary Science Letters*, *193*(3–4), 579–587. https://doi.org/10.1016/S0012-821X(01)00515-5

Yu, J., Day, J., Greaves, M., & Elderfield, H. (2005). Determination of multiple element/calcium ratios in foraminiferal calcite by quadrupole ICP-MS. *Geochemistry, Geophysics, Geosystems*, *6*(8), Q08P01. https://doi.org/10.1029/2005GC000964

References From the Supporting Information

O'Dea, A., Lessios, H. A., Coates, A. G., Eytan, R. I., Restrepo-Moreno, S. A., Cione, A. L., et al. (2016). Formation of the Isthmus of Panama. *Science Advances*, *2*(8), e1600883. https://doi.org/10.1126/sciadv.1600883

Sprintall, J., Gordon, A. L., Koch-Larrouy, A., Lee, T., Potemra, J. T., Pujiana, K., & Wijffels, S. E. (2014). The Indonesian seas and their role in the coupled ocean–climate system. *Nature Geoscience*, *7*(7), 487–492. https://doi.org/10.1038/ngeo2188

Tessler, Z. D., Gordon, A. L., Pratt, L. J., & Sprintall, J. (2010). Transport and dynamics of the Panay Sill overflow in the Philippine Seas. *Journal of Physical Oceanography*, *40*(12), 2679–2695. https://doi.org/10.1175/2010JPO4395.1

Paleoceanography and Paleoclimatology

Supporting Information for

Constraints on Marine Isotope Stage 3 and 5 Sea Level from the Flooding History of the Karimata Strait in Indonesia

Thomas L. Weiss[1,2], Braddock K. Linsley[1], Arnold L. Gordon[1,2], Yair Rosenthal[3,4], and Stefanie Dannenmann-Di Palma[5]

[1]Lamont-Doherty Earth Observatory of Columbia University, 61 Route 9W, Palisades, NY 10964, USA.

[2]Department of Earth and Environmental Science, Columbia University, 557 Schermerhorn Hall Extension, Morningside Campus, New York, NY 10027, USA.

[3]Department of Marine and Coastal Sciences, Rutgers, State University of New Jersey, 71 Dudley Road, New Brunswick, NJ 08901, USA.

[4]Department of Earth and Planetary Sciences, Rutgers University, Busch Campus, 610 Taylor Rd., Piscataway, NJ 08854, USA.

[5]United Nations Office for Disaster Risk Reduction (UNDRR), UN House, Boulevard du Régent 37-40, 1000 Brussels, Belgium

Corresponding author: Thomas Weiss (tweiss@ldeo.columbia.edu.edu)

Contents of this file

Introduction

This document includes additional information on our estimate for the effective depth of the Karimata Strait, a 3-D visualization of Karimata Strait bathymetry and a contour map of the Sunda Shelf, our Mg/Ca data, updated calibration ages for the updated age model, and a summary of where data for core MD97-2141 were published.

Text S1.

Effective Depth of the Karimata Strait

Narrow channels of varied dimensions link ocean basins and seas. This is particularly the situation within the Maritime Continent (MC), with its complex array of seas and channels (Sprintall et al., 2014). The channels serve as conduits for seawater spilling over the topographic sill crest to ventilate deeper basins otherwise isolated from the open ocean (Gordon et al., 2003; Gordon et al., 2011; Tan et al., 2020; Tessler et al., 2010). Above the benthic layer there is along channel, quasi-horizontal flow. Within Karimata Strait there is quasi-horizontal flow (Wang et al., 2019), without an overflow benthic layer.

The amount of water traversing a channel depends on the along channel pressure gradient, wind stress, tidal currents and the fluid viscosity induced by ocean turbulence, including frictional interaction with the sea floor and side-wall boundaries (Tan et al., 2013; Tan et al., 2020). The more restrictive the channel's cross-section area the greater is the bottleneck imprint, as the frictional component. A drop in sea level reduces the cross-section area limiting the along channel transport, which would drop to near zero even before the channel becomes a land bridge (O'dea et al., 2016). The effective sill depth of channel flow is shallower than the topographic sill depth.

The Karimata Strait topographic sill depth is approximately 36 m with a near rectangular cross-section, 100 km wide at the sea surface; 80 km at 20 m depth; 65 km at 30 m depth (Fig. 4). A rectangular cross-section channel would have smaller difference between the effective sill depth and the topographical sill depth than a more restrictive V-shaped cross-section, where the side wall frictional boundary layers merge at the apex.

Presently, a yearly average of about 0.74 Sv in total flows through the Gaspar Strait to the south of Belitung Island and Karimata Strait to the north of the island, with about 2/3 of the total transport through the latter, a wider, deeper channel (Wang et al., 2019). The shallower Gaspar Strait has a V-shaped cross-section offering a more restrictive throughflow passage as sea level drops. Assuming the transport in the narrowest Karimata Strait cross-section (Fig. 4) (which is slightly downstream of the Karimata section presented by Wang et al. (2019)) the average speed through section would be about 0.1 to 0.2 m/sec.

Assuming the along-channel pressure gradient, wind and tidal currents remain the same as they are now, the change in the average speed would increase slightly more than linearly with the drop in sea level, intensifying the frictional retarding effect, acting to reduce the along-channel transport. The average along channel velocity within the Karimata Strait increases to 1.0 m/sec as the sea level drop reaches within 9 m of the topographic sill, to near 2.0 m/sec with a sea level drop to within 5 meters, to 9 m/sec if the water column is near 1 m thick. Assuming a near linear relationship of frictional with along channel velocity, it is expected that the Karimata Strait throughflow transport would be greatly reduced to near zero with a sea level drop of >31 meters, which would be the effective sill depth of Karimata Strait.

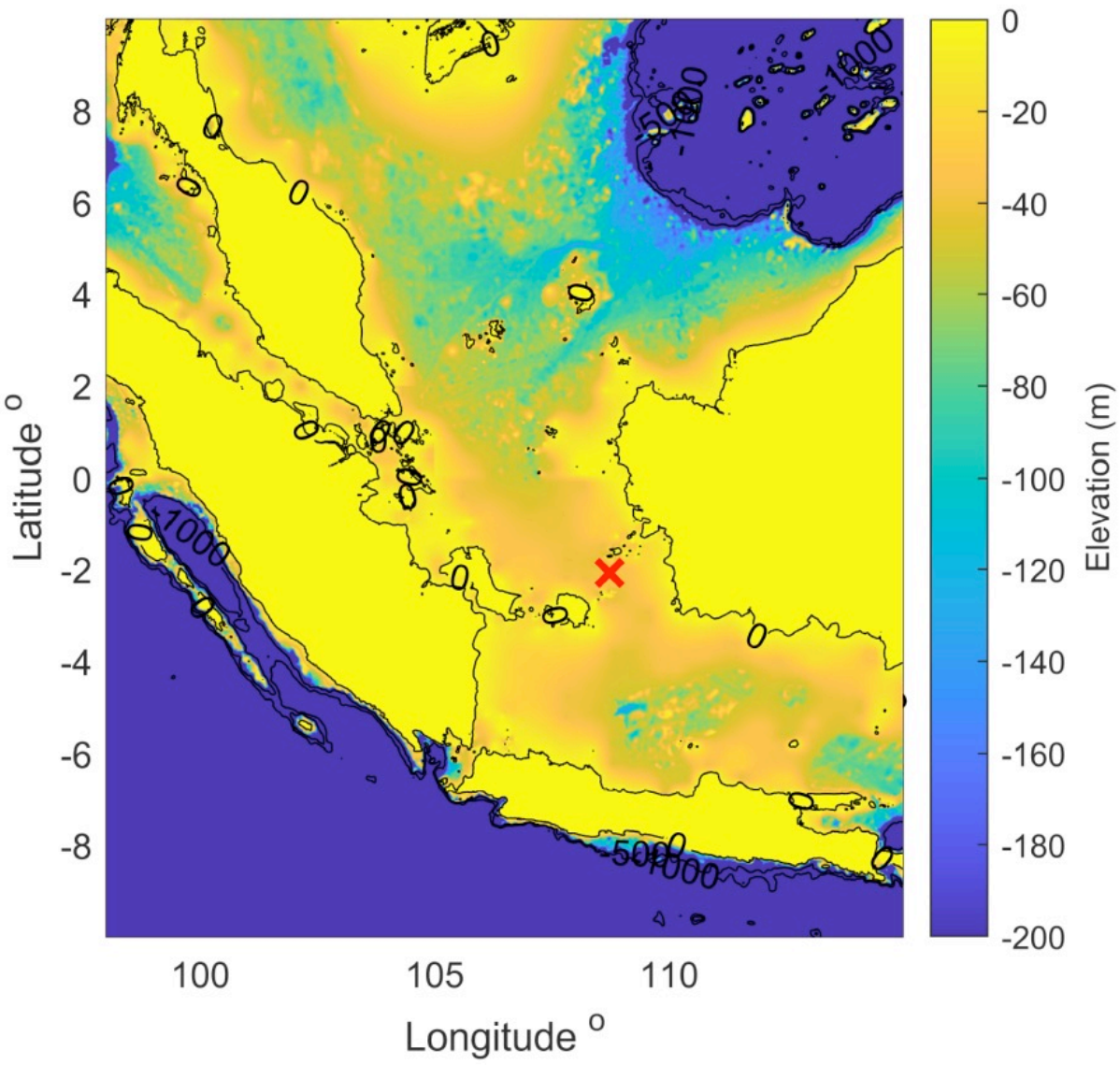

Figure S1. Bathymetry of the Sunda Shelf including the Karimata Strait (red x) (NOAA National Geophysical Data Center, 2009; The NOAA Technical Memorandum:, 2009).

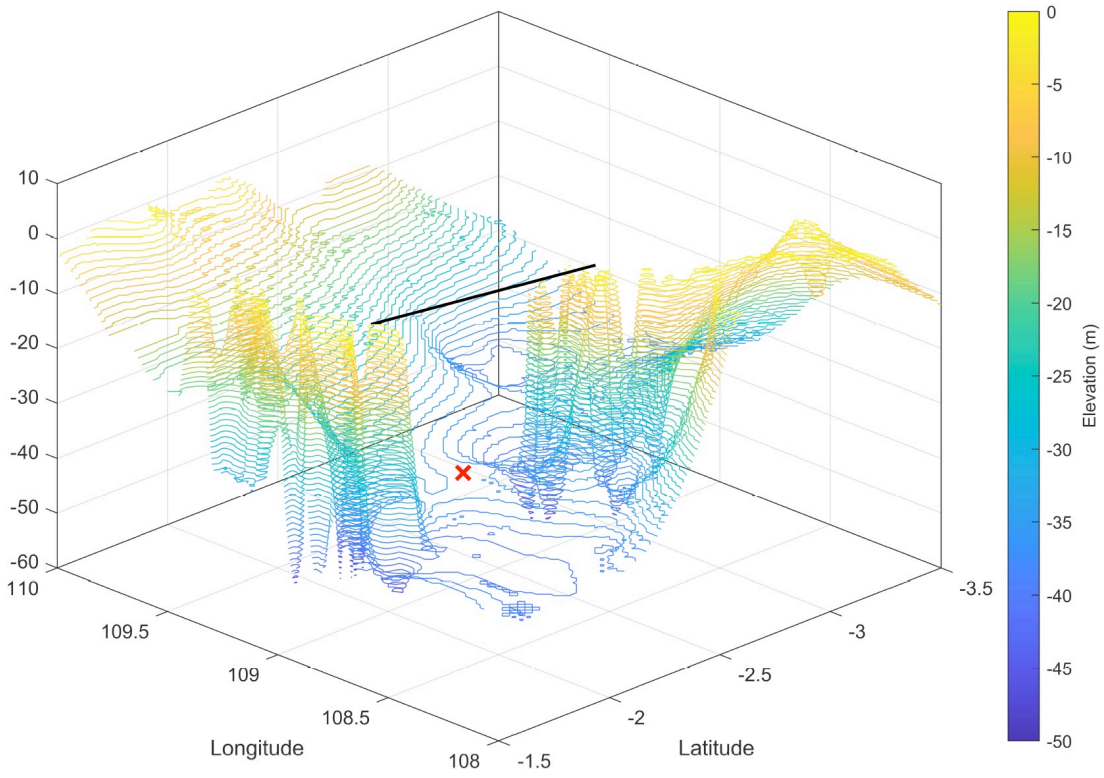

Figure S2. 3-D model of the Karimata Strait (NOAA National Geophysical Data Center, 2009; The NOAA Technical Memorandum:, 2009). The black line and red x are in the same location as in figure 4.

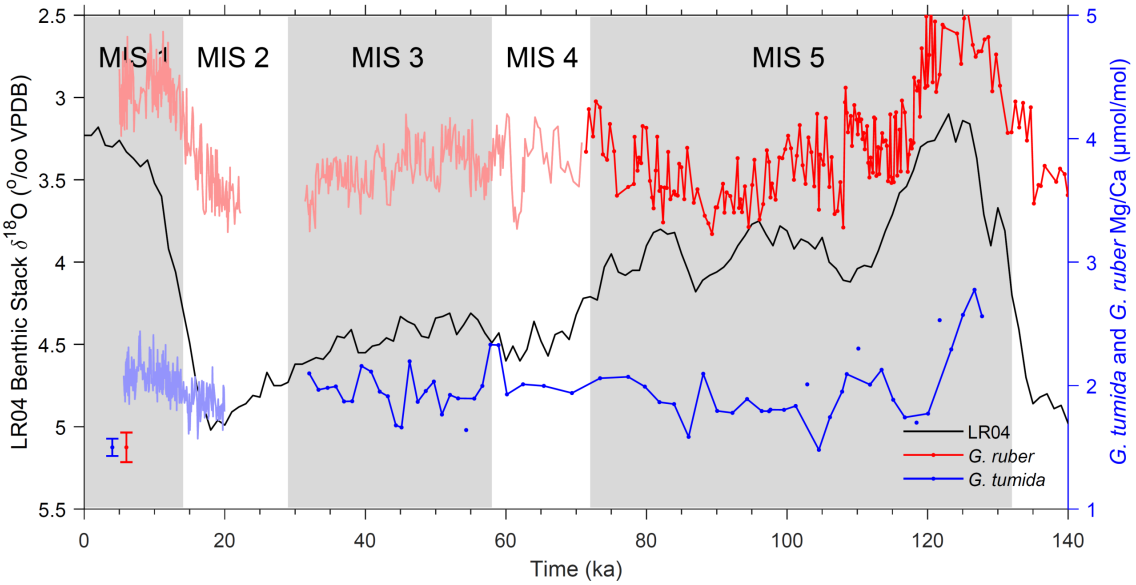

Figure S3. Lisiecki and Raymo (2005) benthic $\delta^{18}O$ stack (black), Sulu Sea *G. ruber* Mg/Ca (red) (Dannenmann et al., 2003; Oppo et al., 2003; Rosenthal et al., 2003a), Sulu Sea *G. tumida* Mg/Ca (blue). Previously published data in plotted in light red and blue, while data published in

this study are in dark red and blue. The five removed *G. tumida* Mg/Ca data are plotted disconnected from the line.

Depth in Core(cm)	AMS 14C Age (yrs bp)	1σ Analytical Error (yrs)	Calibrated Age (yrs bp) (de Garidal Thoron et al., 2001)	Calibrated Age (yrs bp) (This Study)	1σ Minimum Calibrated Age (yrs) (This Study)	1σ Maximum Calibrated Age (yrs) (This Study)
440[a]	28,000	±130	32,101	31,360	31,244	31,366
487[a]	30,900	±260	35,146	34,458	34,215	34,691
506.5	33,000	±310	37,290	36,561	36,117	36,934
543	33,600	±590	37,893	37,398	36,655	38,202
553[a]	34,300	±390	38,790	38,308	37,803	38,831
594[a]	36,900	±460	41,134	41,087	40,664	41,566

Table S1. Recalibrated radiocarbon tie points. Tie points used to generate the age model for de Garidel Thoron et al. (2001) and this study are marked [a].

Species	Data type	Age	Analyses performed by	Data first published in
G. ruber	Mg/Ca	5.01-22.26 ka	Rosenthal, Dannenmann, and Oppo 2003 papers	Rosenthal et al. 2003
G. ruber	Mg/Ca	31.43-70.80 ka	Rosenthal, Dannenmann, and Oppo 2003 papers	Dannenmann et al. 2003
G. ruber	Mg/Ca	71.00-145.38 ka	Rosenthal, Dannenmann, and Oppo 2003 papers	this study
G. ruber	$\delta^{18}O$	5.01-22.26 ka	Rosenthal, Dannenmann, and Oppo 2003 papers	Rosenthal et al. 2003
G. ruber	$\delta^{18}O$	31.43-70.80 ka	Rosenthal, Dannenmann, and Oppo 2003 papers	Dannenmann et al. 2003
G. ruber	$\delta^{18}O$	71.00-145.38 ka	Rosenthal, Dannenmann, and Oppo 2003 papers	Oppo et al., 2003
G. tumida	Mg/Ca	5.63-19.62 ka	Weiss et al. 2021	Weiss et al. 2021
G. tumida	Mg/Ca	32.02-127.75 ka	this study	this study
G. tumida	$\delta^{18}O$	5.01-20.21 ka	Weiss et al. 2021	Weiss et al. 2021
G. tumida	$\delta^{18}O$	31.66-127.75 ka	this study	this study

Table S2. Summary of who generated data and where they were initially published.